Melt migration and chemical differentiation by reactive porosity waves

Annelore Bessat[1], Sébastien Pilet[1], Yuri Y. Podladchikov[1] and Stefan M. Schmalholz[1]

[1] Institute of Earth Sciences, University of Lausanne, 1015 Lausanne, Switzerland

Corresponding author: annelore.bessat@unil.ch

Manuscript submitted to *Geochemistry, Geophysics, Geosystems*

Key Points:

- We present a new thermo-hydro-mechanical-chemical model for melt migration by porosity waves coupled to chemical differentiation
- Chemical differentiation changes the density of solid and melt phases and significantly impacts the melt velocity and evolving porosity
- 2D results of channelized melt migration show a significant chemical exchange between melt and solid, potentially applicable to metasomatism

Abstract

Melt transport across the ductile mantle is essential for oceanic crust formation or intraplate volcanism. Metasomatic enrichment of the lithospheric mantle demonstrates that melts chemically interact with the lithosphere. However, mechanisms of melt migration and the coupling of physical and chemical processes remain unclear. Here, we present a new thermo-hydro-mechanical-chemical (THMC) model for melt migration coupled to chemical differentiation. We study melt migration by porosity waves and consider a simple chemical system of forsterite-fayalite-silica. We solve the one-dimensional (1D) THMC model numerically using the finite difference method. Variables, such as solid and melt densities or MgO and SiO_2 mass concentrations, are fully variable and functions of pressure (P), temperature (T) and total silica mass fraction ($C_T^{\mathrm{SiO_2}}$). These variables are pre-computed with thermodynamic Gibbs energy minimisation, which shows that dependencies of these variables to variations in P, T and $C_T^{SiO_2}$ are considerably different. These P-T-$C_T^{\mathrm{SiO_2}}$ dependencies are implemented in the THMC model via parameterized equations. We consider P and T conditions relevant around the lithosphere-asthenosphere boundary and employ adiabatic and conductive geotherms. Variation of $C_T^{\mathrm{SiO_2}}$ changes the densities of solid and melt and has a strong impact on melt migration. We perform systematic 1D simulations to quantify the impact of initial distributions of porosity and $C_T^{\mathrm{SiO_2}}$ on the melt velocity. An adiabatic gradient generates higher melt velocities. Reasonable values for porosity, permeability, melt and compaction viscosities provide melt velocities between 10 $[\mathrm{cm \cdot yr^{-1}}]$ and 100

[m · yr^{-1}]. We further discuss preliminary results of two 2D simulations showing blob-like and channel-like porosity waves.

Plain Language Summary

Melt transport across the ductile mantle is essential for oceanic crust formation or intraplate volcanism. However, melt transport processes are still incompletely understood and poorly quantified. Xenoliths (inclusions in igneous rock entrained during magma ascent) sampled by kimberlites (an igneous rock that erupted from the mantle) or intraplate basalts provide evidence that there is a chemical interaction (metasomatism) between the rising melt and the solid mantle. However, the impact of chemical processes on melt migration remain unclear. Here, we present a new mathematical two-phase (fluid-solid) model, based on fundamental laws of physics and thermodynamics, which couples melt migration with chemical processes. We study melt migration around the lithosphere/asthenosphere boundary and consider the solid (not molten) rocks as highly viscous fluids due to the high temperatures in these regions (at 80 to 100 km depth). We present one- and two-dimensional results of computer simulations and show that the variation of chemical components, such as silicon dioxide, changes the density of the solid and melt, and can, hence, have a considerable impact on melt migration. We also present two-dimensional simulations, which show the channelization of the rising melt.

1 Introduction

The extraction of melt from its sources and melt transport across the mantle to the surface is a key process in Earth sciences (e.g. McKenzie, 1984; Spiegelman et al., 2001; Keller & Suckale, 2019). The different geodynamic settings with magmatism observed around the world, such as mid-ocean ridges (MORs), volcanic arcs and intraplate volcanism, indicate that asthenospheric melts are extracted under significantly distinct pressure, temperature and rheological conditions. The main difference between melt extraction at intraplate settings and at MORs is the presence of the lithospheric mantle for the intraplate settings. The geochemical signature of MOR basalt (MORB) presumably depends on magma source composition, melt-extraction and differentiation processes intervening between the magma source and the crust (e.g. Langmuir et al., 1992). MORBs are produced and migrate in the asthenosphere and temperature (T) and pressure (P) variations are, hence, controlled by the mantle adiabat. In contrast, asthenospheric melts produced in intraplate settings need to cross the continental or oceanic lithosphere before their extraction to the surface. The lithosphere is characterized by a strong temperature gradient and the associated vertical rheological variations from viscous to elasto-plastic domains (e.g. Burov, 2011). Melt migration in the ductile domain is presumably controlled by porous flow in a viscous solid (McKenzie, 1984), while hydrous fracture propagating into the brittle domain allow melt transport to the surface (e.g. Shaw, 1980; Keller et al., 2013). For intraplate volcanoes, only few studies have focused on the

mechanism of extraction and transport of melt across a thick and cold lithosphere, considering a visco-elasto-plastic deformation behavior (e.g. Keller et al., 2013). Hence, many aspects of the thermo-hydro-mechanical (THM) process of melt migration across the lithosphere remain still little constrained.

In addition to THM processes, melt migration can be affected by chemical (C) reactions, leading to a reactive melt flow (e.g. Jackson et al., 2018). For example, low-viscosity magma, like carbonatite or volatile-rich low degree silicate melts, can rise in the upper mantle. However, such low-degree melts cannot transport significant heat (McKenzie, 1985) and if such melts rise in the lithospheric mantle with a considerable geothermal gradient, then these melts likely interact with the surrounding solid mantle, cool, and crystallize. This melt-solid interaction is frequently referred to as metasomatism and was documented by various xenoliths sampled by kimberlites or intraplate basalts worldwide (e.g. Best, 1974; Lloyd & Bailey, 1975; Francis, 1976; Irving, 1980). Metasomatic processes are important to understand the chemical evolution of the continental lithosphere (e.g. Griffin *et al.*, 2009) and the petrogenesis of alkaline lavas (e.g. Lloyd & Bailey, 1975; Wass & Rogers, 1980, Pilet et al. 2008). However, the origin of the metasomatic agent(s), the process by which low degree melts percolate across the lithosphere, and whether metasomatic processes represent a global mechanism at the asthenosphere-lithosphere boundary (LAB) are still a matter of debate. Therefore, we aim here to investigate coupled THMC processes during melt migration around the LAB.

From a geometrical point of view, there are two general styles of flow during melt migration in a viscous domain: (1) a spatially distributed flow, characterised by a pervasive percolation of melt between the crystals of the solid rock (e.g. olivine or pyroxene crystals in a peridotite) and (2) a spatially focused flow where melt migration is localized in channels, which is documented in the mantle by the presence of metasomatic veins (Wilshire, 1987; Harte et al, 1993). According to the lithosphere thermal gradient, rising melt cools progressively and crystallizes mineral phases which are segregated within the lithospheric mantle, producing metasomatic cumulates sampled by intraplate lavas or observed in mantle outcrops (e.g. Nielson & Noller, 1987; Wilshire, 1987; Nielson & Wilshire, 1993; Harte et al., 1993). Both distributed and focused flows involve a change in the composition of the melt due to its interaction with the solid. For distributed flow, the change of composition is achieved by the infiltrating melt that reacts with the peridotite through an exchange of elements (so-called cryptic metasomatism; Wilshire, 1987). For focused flow, the change in melt composition occurs through differentiation as phases crystallise (so called percolative fractional crystallization; Harte et al., 1993). Most models for the metasomatic enrichment were developed based on observations made in the brittle part of the lithosphere. How metasomatic agents move into the ductile part of the mantle, how such melt interacts with the solid and how channelizing is generated are questions still debated.

From a physical point of view, the rise of large coherent magma bodies in a

viscous solid can be described by diapiric flow (e.g. Cruden, 1988; Weinberg & Podladchikov, 1994; Miller & Paterson, 1999). However, the physical process of melt extraction and migration in partially molten viscous rock is commonly described by two-phase flow models whereby the melt, representing the fluid phase, flows through the pore space of the viscous rock, representing the solid phase (e.g. McKenzie 1984). There are several extraction processes for melt migration in a porous, ductile rock: (1) porous flow, described by Darcy's law, controlled by the rate of melt expulsion whereby the characteristics of solid deformation are of minor importance (e.g. Walker et al. 1978; Ahern & Turcotte, 1979), (2) melt transport by porosity waves for which volumetric deformation of the viscous solid is essential (e.g. McKenzie 1984; Scott & Stevenson 1984; Spiegelman, 1993; Connolly & Podladchikov, 1998; Connolly & Podladchikov, 2007; Keller et al., 2013; Yarushina & Podladchikov, 2015; Omlin et al. 2017; Jordan et al., 2018), (3) melt migration by reaction infiltration instabilities controlled by depth-dependent solubilities (e.g. Aharonov et al., 1995, 1997; Kelemen et al., 1997; Spiegelman et al., 2001; Weatherley & Katz, 2012; Jones & Katz, 2018) and (4) extraction by shear localization and melt segregation generating melt bands (e.g. Stevenson, 1989; Katz et al., 2006; Holtzman & Kohlstedt, 2007). We focus here on melt migration by porosity waves. Connolly & Podladchikov (1998) show that employing a visco-elastic volumetric deformation of the solid enables porosity waves to travel through rock in the limit of zero initial connected porosity. Low-porosity (i.e. few percent) scenarios are most relevant for melt migration across the viscous mantle. The application of decompaction weakening (e.g. Connolly & Podladchikov, 1998, 2007) and the consideration of viscous shear deformation of the solid (Räss et al., 2019) enables a significant channelization of porosity waves for two- and three-dimensional (2D and 3D) flow. Furthermore, Omlin et al. (2017) show that the coupling of the kinetics of chemical reactions with fluid flow may enable porosity waves also to potentially arise in low-temperature regimes, so that the porosity waves are not necessarily limited to the high-temperature viscous regions (Chakraborty, 2017). Moreover, Jordan et al. (2018) show that mass, and hence melt, can be transported in 2D and 3D porosity waves; a fact that has been doubted based on 1D porosity wave studies. Therefore, porosity waves are a potential mechanism to transport significant melt in a channelized style across the LAB and the viscous lithospheric mantle.

Here, we present a new numerical THMC model to investigate reactive melt migration by porosity waves in a viscous solid coupled to heat transfer and to chemical differentiation of major elements in the melt and solid. Chemical differentiation of major elements is important for melt migration because it changes the density of the melt and solid. Such density variations do not occur for trace element transport by porosity waves (e.g. Jordan et al., 2018) applied to study, for example, the chromatographic separation occurring during percolation (Korzhinskii, 1965; Hofmann, 1972), because trace elements do not alter the density of melt and solid. The importance of chemical differentiation for the rise of magma in the crust has been highlighted recently by Jackson et al.

(2018). We couple our THMC model with thermodynamic results calculated by Gibbs energy minimisation. We perform this minimisation with a self-developed MATLAB code using a linear programming algorithm. The P and T conditions are chosen to reflect conditions at the LAB. We consider a simple ternary system composition of MgO, FeO and SiO_2 based on the olivine phase diagram system, forsterite (Mg_2SiO_4) and fayalite (Fe_2SiO_4). We consider conditions for which the system is always between solidus and liquidus so that both melt and solid phase are present simultaneously. We extend this binary system by adding more SiO_2 using experimental data of peridotite in equilibrium with melt at 3 GPa (Davis et al., 2011). All model variables determined by thermodynamic calculations (e.g. solid and melt densities, mass fractions of MgO and SiO_2 of the melt and the solid) are a function of P, T and chemical SiO_2 composition of the system ($C_T^{\mathrm{SiO_2}}$). These variables and their dependence of P, T and SiO_2 are precomputed and used in the THMC reactive transport model, so that they can evolve freely with evolving P, T and SiO_2. The model, hence, allows quantifying the impact of variations in the chemical composition on melt migration.

The aims of this study are (i) to present a new numerical THMC-thermodynamic model for coupled melt migration and chemical differentiation by reactive porosity waves, (ii) to explain specific features of coupling chemical differentiation with porosity waves and (iii) to discuss potential applications of our model to melt migration around the LAB. We present the model derivation and some systematic results for 1D and show two representative results for 2D showing blob- and channel-type reactive porosity waves.

2 Mathematical model

We develop a 1D mathematical model for THMC reactive transport by porosity waves. The model is based on the concepts of continuum mechanics, two-phase flow and equilibrium thermodynamics and follows the same approach in deriving a closed system of equations as described in Yarushina & Podladchikov (2015), Malvoisin et al. (2015) or Schmalholz et al. (2020). The complete THMC model consists of two parts: a THMC model for reactive transport of melt by porosity waves, consisting of a system of partial differential equations, and a thermodynamic model, based on Gibbs energy minimisation, which provides the required solid and melt densities, solid and melt mass fractions of MgO and SiO_2, and solid and melt thermal energies, and their respective dependencies on P, T and $C_T^{\mathrm{SiO_2}}$.

2.1 Thermodynamic model

We apply a thermodynamic model to determine the stable phases for a range of P, T and composition (X). We start with a simple binary system of olivine (Fig. 1a) between forsterite, the olivine magnesium-rich end-member (Mg_2SiO_4), and fayalite, the olivine iron-rich end-member (Fe_2SiO_4).

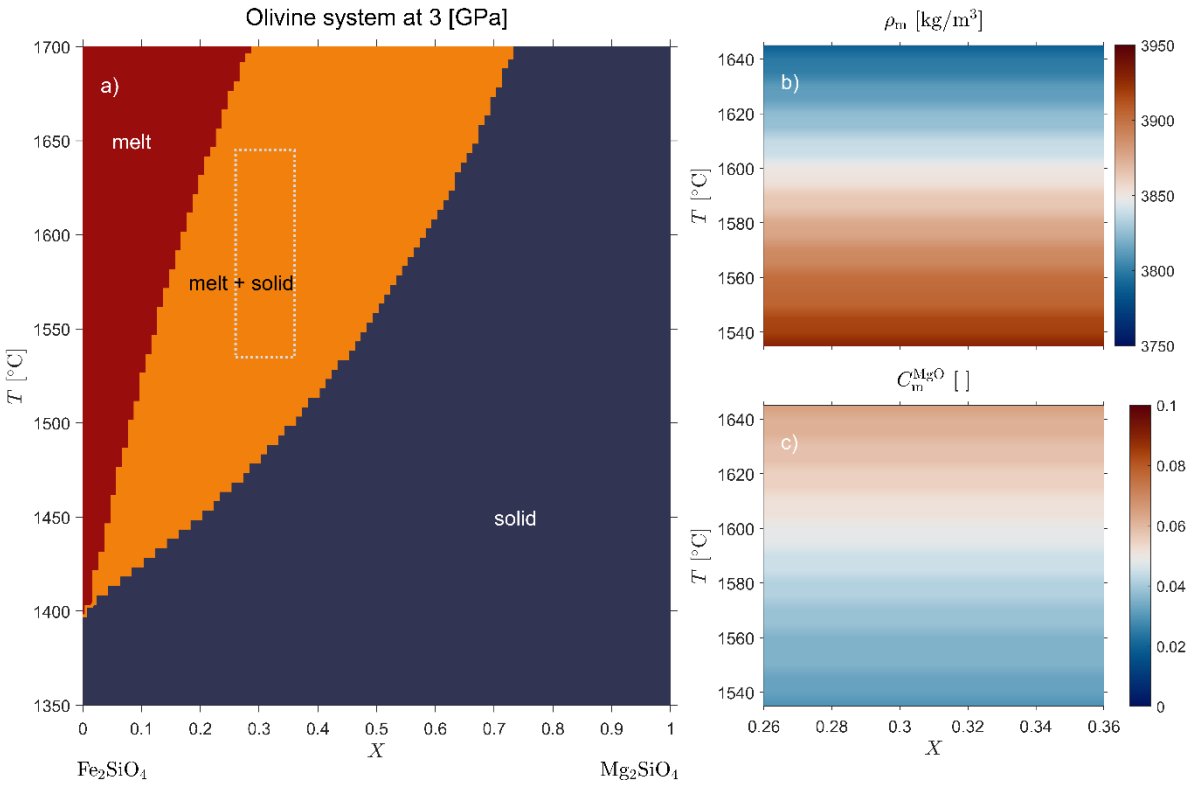

Figure 1. Panel (a) shows the binary system of olivine for a pressure of 3 GPa. Blue area shows where solid is stable, red area shows where melt is stable and orange area shows where both solid and melt are stable. Dashed square indicates the region used to calculate thermodynamic variables employed in the THMC model. Panels (b) and (c) show respectively, the melt density and the melt mass fraction of magnesium (in the dashed region), which are independent on X in the region of interest.

We minimize the Gibbs free energy, G, to determine the equilibrium of the binary system. The Gibbs free energies used for the minimisation are from the thermodynamic database of Holland & Powell (1998). To calculate this minimisation, we use the linear programming "linprog" algorithm from MATLAB. We consider a pressure range of 0.1 GPa to 4.9 GPa and a temperature range of 1'200 °C to 1'700 °C. The X composition varies from 0 to 1, with 0 corresponding to 100% of fayalite and 0% of forsterite and 1 corresponding to 0% fayalite and 100% of forsterite. There are four mineral phases for this solid-melt system; for the solid part there are forsterite (fo) and fayalite (fa) as well as for the melt (liquid) part there are forsterite (foL) and fayalite (faL) (see Hollande & Powell, 1998 for nomenclature). Figure 1a shows the result of the minimisation and emphasizes where the phases are stable for a pressure of 3 GPa. After

the minimisation of G, in each point of the P-T-X domain, we extract several quantities for the melt (with subscript m) and the solid (with subscript s; all listed in Table 1): Gibbs energy, G_m and G_s in [J mol^{-1}], volume, V_m and V_s in [m^3 mol^{-1}], entropy, S_m and S_s in [J mol^{-1} K^{-1}] and specific heat capacity, c_{p_m} and c_{p_s} in [J mol^{-1} K^{-1}]. We calculate the extensive quantities from the Gibbs energies, volume $V_{m,s} = \frac{dG_{m,s}}{\mathrm{dP}}$ and entropy $S_{m,s} = -\frac{dG_{m,s}}{\mathrm{dT}}$. The specific heat capacity $c_{p_{m,s}} = T \frac{dS_{m,s}}{\mathrm{dT}}$. To have all parameters in mass units of kilogram, and not in mole, we divide all quantities by their respective melt or solid molar mass, m_m and m_s in [kg mol^{-1}]. With the volume per unit mass, we can then calculate melt and solid density, $\rho_{m,s} = \frac{1}{V_{m,s}}$ in [kg m^{-3}]. In addition, several molar fractions (in mole units) can be obtained from Gibbs minimisation, like melt concentrations of forsterite and fayalite, $C^{\mathrm{foL}}_{m,[\mathrm{mol}]}$ and $C^{\mathrm{faL}}_{m,[\mathrm{mol}]}$, and solid concentrations of forsterite and fayalite, $C^{\mathrm{fo}}_{s,[\mathrm{mol}]}$ and $C^{\mathrm{fa}}_{s,[\mathrm{mol}]}$. We transform them into mass fractions in order to use them in the mass conservation equations of the THMC model. The details of this transformation are presented in Appendix C, equations C1 to C3.

In the solid-melt THMC model, we focus on the thermodynamic region where melt and solid coexist (orange area in Fig. 1a). In the considered P-T-X domain, this region has a pressure range of 2.4001 GPa to 3.5001 GPa, a temperature range of 1'535°C (1'808.15 K) to 1'645°C (1'918.15 K) and a composition range of 0.26 to 0.36. Figures 1b and 1c show that the variation in melt density (ρ_m) and in melt mass fraction of magnesium (C_m^{MgO}), respectively, are independent of composition in this range. Accordingly, all other thermodynamic parameters used in the THMC model are also independent of composition, such as solid density (ρ_s), solid mass fraction of magnesium (C_s^{MgO}) and melt and solid mass fractions of silica ($C_m^{\mathrm{SiO_2}}$, $C_s^{\mathrm{SiO_2}}$). Therefore, we can reduce our binary P-T-X domain to a P-T domain for all considered parameters. The independency of densities and mass fractions on composition X is a result of the Gibbs phase rule (e.g. Müller, 2007) because there is no degree of freedom for a system with two components (fo and fa) and two phases (solid and melt) for a given temperature and pressure. Figure 2 shows the variation of thermodynamic parameters used in the THMC code as function of temperature and pressure. All parameters show an essentially linear variation with P and T (Figure 2).

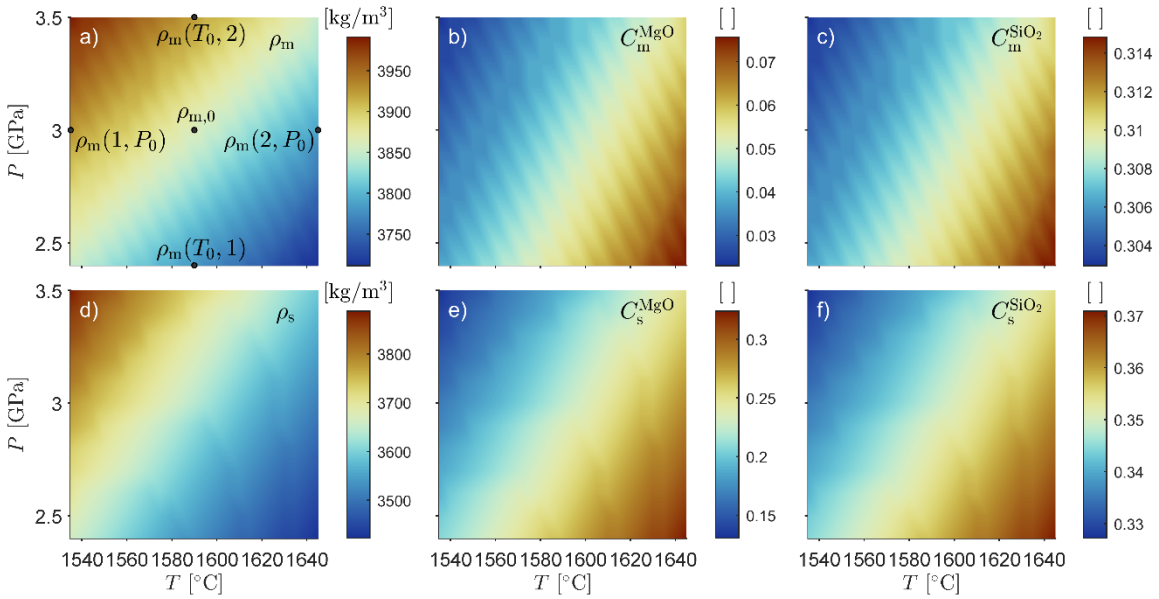

Figure 2. Variation of thermodynamic variables used in the THMC transport code. Variables are calculated by Gibbs free energy minimization. Enlargement of the region of coexistence between melt and solid (orange area in Fig. 1a). All parameters depend on temperature and pressure: panel (a) for melt density, panel (d) for solid density, panel (b) for mass fraction of magnesium in melt, panel (e) for mass fraction of magnesium in solid, panel (c) for mass fraction of silica in melt and panel (f) for mass fraction of silica in solid. Black points in panel (a) are used to calculate α and β in equations 1 and 2.

The essentially linear variation allows making a linear approximation for all six parameters by calculating two values, α and β, whereby α quantifies the variation of a variable with respect to a variation of temperature, for a constant pressure of reference P_0, and β quantifies the variation of the variable with respect to a variation of pressure, for a constant temperature of reference T_0. The α and β for the six variables are calculated, for example, for the melt density by (see Fig.2a for details):

$$\alpha_{\rho_m} = \frac{\left(\frac{\rho_m(2,P_0)-\rho_m(1,P_0)}{T}\right)}{\rho_{m,0}} \quad (1)$$

$$\beta_{\rho_m} = \frac{\left(\frac{\rho_m(T_0,2)-\rho_m(T_0,1)}{P}\right)}{\rho_{m,0}} \quad (2)$$

where T and P are the temperature and pressure differences of domain P-T, $\rho_m(2,P_0) - \rho_m(1,P_0)$ is density variation as function of temperature, $\rho_m(T_0,2) - \rho_m(T_0,1)$ is density variation as function of pressure and $\rho_{m,0}$ is

the density at the reference point T_0 and P_0. The same procedure is applied for the other five variables: the resulting α, β and corresponding reference points are given in Table 2 and further discussed in the result section. Figure 3 shows the results of this approximation for each variable.

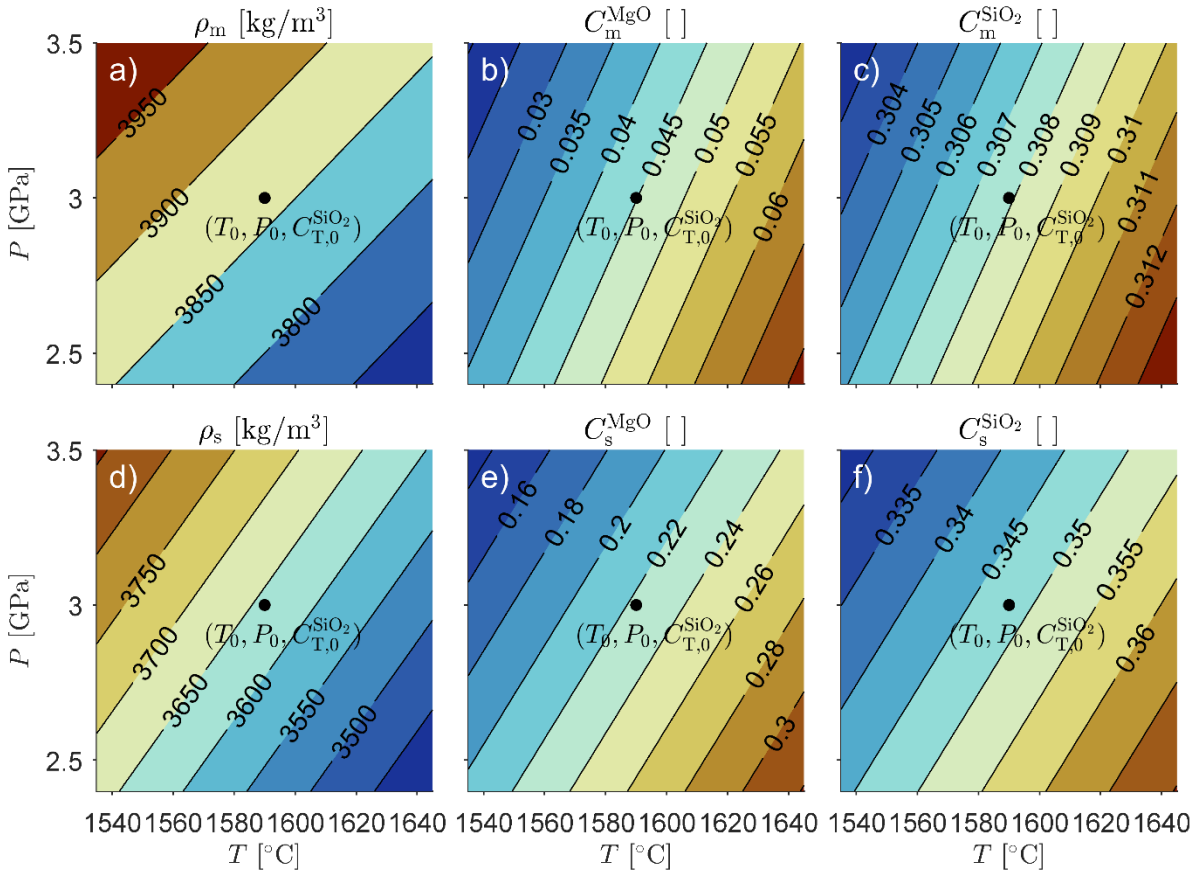

Figure 3. Linear approximation of data obtained by thermodynamics with α and β. All variations are in function of temperature and pressure: panel (a) for melt density, panel (d) for solid density, panel (b) for mass fraction of magnesium in melt, panel (e) for mass fraction of magnesium in solid, panel (c) for mass fraction of silica in melt and panel (f) for mass fraction of silica in solid. Black point in the centre of each panel is the reference point at T_0, P_0 and $C_{T,0}^{SiO_2}$. $C_{T,0}^{SiO_2}$corresponds to the total mass fraction of silica in the olivine.

A particular result for olivine in the considered pressure and temperature range is that solid density is smaller than melt density (Figs. 2 and 3). This is a known phenomenon in the forsterite-fayalite system for high temperature (e.g. Herzberg et al., 1982). For melt to rise, it should have a smaller density than the

solid. To obtain smaller melt densities, we add another composition dimension to our P-T domain, which is the total silica mass fraction $C_T^{\mathrm{SiO_2}}$. Adding more silica to the olivine system allows to change the melt and solid densities of the system to a more realistic value for a peridotitic system. For simplicity, we did not included pyroxenes in our thermodynamic calculation.

The total silica mass fraction ($C_T^{\mathrm{SiO_2}}$) is calculated at the reference point T_0 and P_0 as follows:

$$C_{T,0}^{\mathrm{SiO_2}} = \frac{C_{m,0}^{\mathrm{SiO_2}} + C_{s,0}^{\mathrm{SiO_2}}}{C_{m,0}^{\mathrm{MgO}} + C_{s,0}^{\mathrm{MgO}} + C_{m,0}^{\mathrm{FeO}} + C_{s,0}^{\mathrm{FeO}} + C_{m,0}^{\mathrm{SiO_2}} + C_{s,0}^{\mathrm{SiO_2}}} \tag{3}$$

By increasing the total silica mass fraction, the density of melt will become smaller than the density of solid, allowing the melt to percolate towards the surface. We use an experiment by Davis et al. (2011) which provides the composition of a peridotite in equilibrium with the first magma produced by partial melting at a pressure of 3 GPa and a temperature of 1'450 °C. These experimental compositions are reported as "KLB-1ox" for the solid, and "0% melt" for melt in Table 1 of Davis et al. (2011). The combination of these data and the values obtained by our thermodynamic olivine model allows calculating a γ parameter that quantifies the variation of the six variables, ρ_m, ρ_s, C_m^{MgO}, C_s^{MgO}, $C_m^{\mathrm{SiO_2}}$, $C_s^{\mathrm{SiO_2}}$, as function of the total silica mass fraction in the system. To calculate γ for mass fractions of magnesium or silica for melt and solid, we transform MgO, FeO and SiO_2 oxides weight percent of "KLB-1ox" and "0% melt" into oxides mass fractions (here shown for MgO, same procedure for FeO and SiO_2):

$$C_{m,exp}^{\mathrm{MgO}} = \frac{C_{0\%\ melt,\ [wt\%]}^{\mathrm{MgO}}}{C_{0\%\ melt,\ [wt\%]}^{\mathrm{MgO}} + C_{0\%\ melt,\ [wt\%]}^{\mathrm{FeO}} + C_{0\%\ melt,\ [wt\%]}^{\mathrm{SiO_2}}} \tag{4a}$$

$$C_{s,exp}^{\mathrm{MgO}} = \frac{C_{KLB-1ox,\ [wt\%]}^{\mathrm{MgO}}}{C_{KLB-1ox,\ [wt\%]}^{\mathrm{MgO}} + C_{KLB-1ox,\ [wt\%]}^{\mathrm{FeO}} + C_{KLB-1ox,\ [wt\%]}^{\mathrm{SiO_2}}} \tag{4b}$$

The total silica mass fraction of the experiment, $C_{T,exp}^{\mathrm{SiO_2}}$, is calculated in the same way as shown in equation 3. Then we calculate the γ (here shown for C_m^{MgO} and C_s^{MgO}, same procedure for $C_m^{\mathrm{SiO_2}}$ and $C_s^{\mathrm{SiO_2}}$ shown in Appendix C, equation C4) by:

$$\gamma_{C_m^{\mathrm{MgO}}} = \frac{\left(\frac{C_{m,exp}^{\mathrm{MgO}} - C_{m,0}^{\mathrm{MgO}}}{C_{T,exp}^{\mathrm{SiO_2}} - C_{T,0}^{\mathrm{SiO_2}}} \right)}{C_{m,0}^{\mathrm{MgO}}} \tag{5a}$$

$$\gamma_{C_s^{\mathrm{MgO}}} = \frac{\left(\frac{C_{s,exp}^{\mathrm{MgO}} - C_{s,0}^{\mathrm{MgO}}}{C_{T,exp}^{\mathrm{SiO_2}} - C_{T,0}^{\mathrm{SiO_2}}} \right)}{C_{s,0}^{\mathrm{MgO}}} \tag{5b}$$

To calculate γ for melt and solid densities we proceed in the same way:

$$\gamma_{\rho_m} = \frac{\left(\frac{\rho_{m,exp}-\rho_{m,0}}{C_{T,exp}^{\mathrm{SiO_2}}-C_{T,0}^{\mathrm{SiO_2}}}\right)}{\rho_{m,0}} \quad (6a)$$

$$\gamma_{\rho_s} = \frac{\left(\frac{\rho_{s,exp}-\rho_{s,0}}{C_{T,exp}^{\mathrm{SiO_2}}-C_{T,0}^{\mathrm{SiO_2}}}\right)}{\rho_{s,0}} \quad (6b)$$

The values for the melt and solid densities, $\rho_{m,exp}$ and $\rho_{s,exp}$, are not provided in Davis et al. (2011). We calculate these densities using the values included in our thermodynamic data base and the mineral mode reported in Table 1 of Davis et al. (2011) (see Appendix C for the detail of these calculations).

Figure 4 shows the linear approximation using γ for the different variables between the forsterite-fayalite binary olivine system, $C_{T,0}^{\mathrm{SiO_2}} = 0.33$, and the experiment of Davis et al. (2011), $C_{T,experiment}^{\mathrm{SiO_2}} = 0.56$. Figure 4a shows the relative change of solid and melt densities and the value of $C_T^{\mathrm{SiO_2}} = 0.41$, indicated by the vertical black dashed line, for which melt and solid densities are equal.

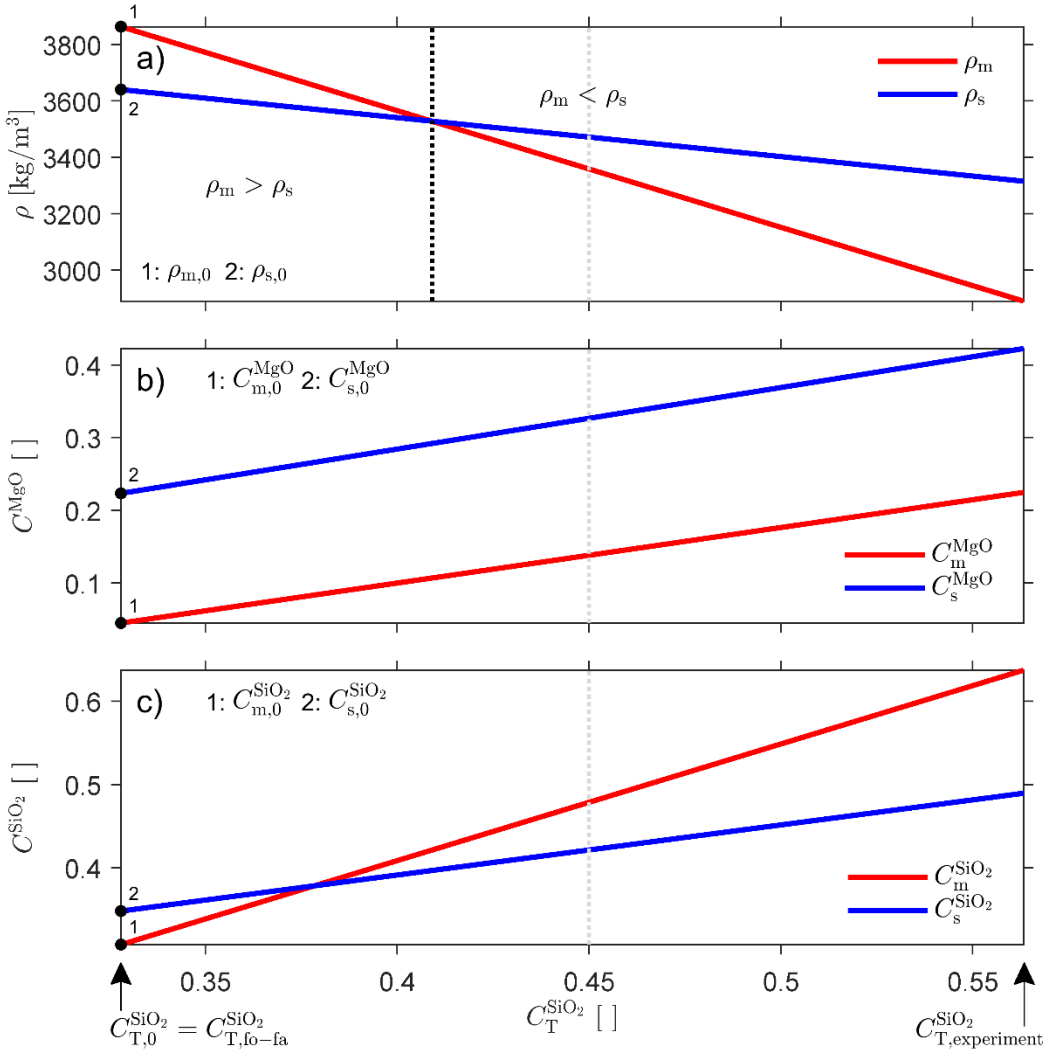

Figure 4. Linearized dependence of thermodynamic variables on total silica mass fraction, $C_T^{SiO_2}$. Panel (a) densities, melt in red and solid in blue, panel (b) mass fractions of magnesium, melt in red and solid in blue and panel (c) mass fractions of silica, melt in red and solid in blue. Black points are reference values of each variable at T_0, P_0 and $C_{T,0}^{SiO_2}$ in Figure 3. $C_{T,experiment}^{SiO_2}$ corresponds to the total mass fraction of silica in the experiment of Davis et al. (2011). The black dashed line indicates at which total silica mass fraction the melt density becomes smaller than the solid density. The grey dashed line shows the value selected in the THMC model as the initial total silica mass fraction.

To calculate the melt and solid thermal energies, U_m and U_s, required for the temperature calculation, we only consider, for simplicity, their variation with

respect to temperature and density. We use values for the respective melt and solid specific heat at the reference point T_0 and P_0, $c_{p_{m,0}}$ and $c_{p_{s,0}}$ (values are given in Table 2) and calculate the thermal energies by:

$$U_m = \rho_m \cdot c_{p_{m,0}} \cdot T \quad (7a)$$

$$U_s = \rho_s \cdot c_{p_{s,0}} \cdot T \quad (7b)$$

We apply this simplification of the thermal solid and melt energies because in our model the temperature deviation from the initial thermal gradient is small because we remain in the region of coexistence of melt and solid.

In summary, the thermodynamic model calculates eight variables: solid and melt densities, solid and melt mass fractions of MgO and SiO_2, and solid and melt specific heat. The densities and mass fractions are all a function of pressure, temperature and total SiO_2 concentration and these dependencies will be quantified below by a total of 18 parameters, namely 6 different values each for α, β and γ (Table 2). These 18 parameters will be used in the THMC transport model.

Table 1. Parameters used in the thermodynamic and THMC model

Symbol	Meaning	Units
ρ_m, ρ_s, ρ_T	melt, solid and total densities	$kg \cdot m^{-3}$
C_m^{MgO}, C_s^{MgO}, $C_m^{SiO_2}$, $C_s^{SiO_2}$	mass fractions of magnesium or silica for melt and solid	[ ]
U_m, U_s	melt, solid thermal energies	$J \cdot mol^{-1}$
c_{p_m}, c_{p_s}	melt, solid specific heat capacity	$J \cdot kg^{-1} \cdot K^{-1}$
λ_m, λ_s, λ_T	melt, solid and total thermal conductivity	$W \cdot m^{-1} \cdot K^{-1}$
G_m, G_s	melt, solid Gibbs energies	$J \cdot mol^{-1}$
V_m, V_s	melt, solid volumes	$m^3 \cdot mol^{-1}$
S_m, S_s	melt, solid entropy	$J \cdot mol^{-1} \cdot K^{-1}$
m_m, m_s	melt, solid molar mass	$kg^1 \cdot mol^{-1}$
k	Permeability	m^2
φ	Porosity	[ ]
v_m, v_s	melt, solid velocity	$m \cdot s^{-1}$
σ_{xx}	total stress	Pa
τ	deviatoric stress	Pa
g	gravitational acceleration	$m \cdot s^{-2}$
P_T, P_m, P_e	total pressure, melt pressure and effective pressure	Pa
η_s, η_v, η_m	shear viscosity, compaction viscosity and melt viscosity	$Pa \cdot s$
t	Time	s
T	Temperature	K

2.2 Thermo-Hydro-Mechanical-Chemical model

The applied THMC model is based on a system of conservation equations. The general derivation of these conservation equations is given in the appendix and below only the applied equations are given. The conservation of total mass is

$$\frac{\partial}{\partial t}\left(\rho_m\varphi + \rho_s(1-\varphi)\right) = -\frac{\partial}{\partial x}\left(\rho_m\varphi v_m + \rho_s(1-\varphi)v_s\right) \quad (8)$$

where t is the time, φ is the porosity, x is the spatial coordinate (here the direction parallel to gravity) and v_m and v_s are the melt and solid velocity, respectively. The equation of conservation of total mass of MgO is

$$\frac{\partial}{\partial t}\left(C_m^{\mathrm{MgO}}\rho_m\varphi + C_s^{\mathrm{Mg}O}\rho_s(1-\varphi)\right) = -\frac{\partial}{\partial x}\left(C_m^{\mathrm{Mg}O}\rho_m\varphi v_m + C_s^{\mathrm{Mg}O}\rho_s(1-\varphi)v_s\right) \quad (9)$$

and of conservation of total mass of SiO_2 is

$$\frac{\partial}{\partial t}\left(C_m^{\mathrm{SiO_2}}\rho_m\varphi + C_s^{\mathrm{SiO_2}}\rho_s(1-\varphi)\right) = -\frac{\partial}{\partial x}\left(C_m^{\mathrm{SiO_2}}\rho_m\varphi v_m + C_s^{\mathrm{SiO_2}}\rho_s(1-\varphi)v_s\right) \quad (10)$$

For the conservation of the total masses of MgO and SiO_2, we consider only the advective part of the conservation equation because we assume that diffusion processes are much slower than advection processes (corresponding Péclet number » 1). The conservation of thermal energy is

$$\frac{\partial}{\partial t}\left(U_m\varphi + U_s(1-\varphi)\right) = -\frac{\partial}{\partial x}\left(U_m\varphi v_m + U_s(1-\varphi)v_s - \lambda_T\frac{\partial T}{\partial x}\right) \quad (11)$$

where $\lambda_T = (\lambda_m\varphi + \lambda_s(1-\varphi))$ and λ_m and λ_s are the thermal conductivity of melt and solid, respectively. The conservation of linear momentum of the solid is given by

$$\frac{\partial\sigma_{\mathrm{xx}}}{\partial x} = \rho_T g \quad (12)$$

where σ_{xx} is the total stress, $\rho_T = \rho_m\varphi + \rho_s(1-\varphi)$ is the total density and g is the gravitational acceleration. The total stress is given by

$$\sigma_{\mathrm{xx}} = -P_T + \tau \quad (13)$$

where P_T is the total pressure (i.e. the mean stress) and τ is the deviatoric stress. The conservation of linear momentum of fluid, also known as Darcy's law, is given by

$$\varphi\,(v_m - v_s) = -\frac{k\varphi^3}{\eta_m}\left(\frac{\partial P_m}{\partial x} + \rho_m g\right) \quad (14)$$

where k is the permeability coefficient in a Kozeny-Carman type model, η_m is the melt viscosity and P_m is the melt pressure. We use the melt pressure as thermodynamic pressure for the thermodynamic calculations. The system is closed by two constitutive equations. The first equation is used to calculate the total pressure,

$$P_T = P_m - \frac{\partial v_s}{\partial x}(1-\varphi)\eta_v \quad (15)$$

where η_v is the solid volumetric viscosity (i.e. compaction viscosity). We consider in the equation for P_T only a viscous volumetric deformation since an additional reversible elastic volumetric deformation is generated by the considered thermodynamic reactions, specifically the variation of density with melt pressure. Temporal variations of P_m are related via a compressibility, β, to temporal variations of the densities (Table 2 and eq. 2). These density variations are considered in the mass conservation equations and, hence, affect the volumetric deformation. Therefore, the temporal variation of P_m is indirectly related via the compressibility and density to the divergence of solid velocities, which effectively corresponds to a reversible elastic relation between melt pressure and divergence of solid velocity (e.g. $\beta\frac{\partial P_m}{\partial t} = -\frac{\partial v_s}{\partial x}$). Elastic volumetric deformation is, hence, considered indirectly in our THMC model by the consideration of reversible equilibrium reactions. The second constitutive equation is used to calculate τ by

$$\tau = 2\eta_s \frac{\partial v_s}{\partial x} \quad (16)$$

where η_s is the shear viscosity of the solid. For more details on the development of all equations, see Appendix A.

2.3 Coupled THMC and thermodynamic model and numerical method

The entire system of equations describing the THMC and thermodynamic models has a total of 14 unknowns; 8 unknowns are determined by the thermodynamic model, namely ρ_m, ρ_s, C_m^{Mgo}, C_s^{Mgo}, $C_m^{\mathrm{SiO_2}}$, $C_s^{\mathrm{SiO_2}}$, U_m and U_s, and 6 unknowns are determined by the THMC model, namely P_m, φ, $C_T^{\mathrm{SiO_2}}$, T, v_m,

v_s. In the thermodynamic model the unknowns are determined by T, P_m and $C_T^{\mathrm{SiO_2}}$ using pre-computed results from Gibbs energy minimizations (i.e. phase diagrams of the 8 thermodynamic variables) whereas in the THMC model the unknowns are calculated by numerically solving a system of coupled partial differential equations.

We use a standard staggered grid finite difference (FD) method (e.g. Gerya 2019) to solve the partial differential equations of the THMC model. The numerical algorithm consists of a standard time loop with an internal pseudo-transient (PT) iterative loop to determine P_m, φ, $C_T^{\mathrm{SiO_2}}$, T and v_s. This PT method (e.g. Duretz et al. 2019; Räss et al. 2019; Schmalholz et al. 2020) solves nonlinear system of equations in an iterative way without the need of inverting a numerical coefficient matrix. To use the PT method, we transform the conservation equations in pseudo-transient equations by adding a pseudo-transient time derivative, with PT time step t^{PT}, for each unknown variable, P_m, φ, $C_T^{\mathrm{SiO_2}}$, T and v_s. The PT equations are

$$\frac{\partial P_m}{\partial\, t_P{}^{\mathrm{TP}}} = -\frac{\partial}{\partial t}\left(\rho_m\varphi + \rho_s(1-\varphi)\right) - \frac{\partial}{\partial x}\left(-\rho_m \frac{k\varphi^3}{\eta_m}\left(\frac{\partial P_m}{\partial x} + \rho_m g\right) + \rho_T v_s\right) \tag{17a}$$

$$\frac{\partial \varphi}{\partial\, t_\varphi{}^{\mathrm{TP}}} = -\frac{\partial}{\partial t}\left(C_m^{\mathrm{MgO}}\rho_m\varphi + C_s^{\mathrm{MgO}}\rho_s(1-\varphi)\right) - \frac{\partial}{\partial x}\left(C_m^{\mathrm{MgO}}\rho_m\varphi v_m + C_s^{\mathrm{MgO}}\rho_s(1-\varphi)v_s\right) \tag{17b}$$

$$\frac{\partial C_T^{\mathrm{SiO_2}}}{\partial\, t_{C_T^{\mathrm{SiO_2}}}{}^{\mathrm{TP}}} = -\frac{\partial}{\partial t}\left(C_m^{\mathrm{SiO_2}}\rho_m\varphi + C_s^{\mathrm{SiO_2}}\rho_s(1-\varphi)\right) - \frac{\partial}{\partial x}\left(C_m^{\mathrm{SiO_2}}\rho_m\varphi v_m + C_s^{\mathrm{SiO_2}}\rho_s(1-\varphi)v_s\right) \tag{17c}$$

$$\frac{\partial T}{\partial\, t_T{}^{\mathrm{TP}}} = -\frac{\partial}{\partial t}\left(U_m\varphi + U_s(1-\varphi)\right) - \frac{\partial}{\partial x}\left(U_m\varphi v_m + U_s(1-\varphi)v_s - \lambda_{\mathrm{tot}}\frac{\partial T}{\partial x}\right) \tag{17d}$$

$$\frac{\partial v_s}{\partial\, t_{v_s}{}^{\mathrm{TP}}} = \frac{\partial}{\partial x}\left(-P_T + \tau\right) - \rho_T g \tag{17e}$$

When the PT time derivatives on the left-hand sides of the above equation are zero, the corresponding equations of the right-hand side are solved. In practice, the iteration will continue in the PT iteration loop as long as PT time derivatives are not smaller than a specified numerical tolerance error. In the FD method, we use numerical time steps representing the physical time step t to approximate the time derivatives, which control the physical time evolution (i.e. the "real" time derivatives). We employ five PT time steps to solve for P_m, $t_P{}^{\mathrm{TP}}$, for φ, $t_\varphi{}^{\mathrm{TP}}$, for $C_T^{\mathrm{SiO_2}}$, $t_{C_T^{\mathrm{SiO_2}}}{}^{\mathrm{TP}}$, for T, $t_T{}^{\mathrm{TP}}$ and for v_s, $t_{v_s}{}^{\mathrm{TP}}$. The choice of these numerical PT time steps is crucial for a stable convergence of the PT iterative solution but does not affect the result after the convergence. The values of the PT time steps are given in Appendix B, Table B3. The melt velocity can be directly calculated from Darcy's law (eq. 14), which does not require the solution of an additional differential equation.

2.4 Model configuration and characteristic values

The algorithm is programmed in such way that most parameters have magnitudes close to 1. This approach was extremely useful to determine the best possible numerical stability and convergence of the pseudo-transient algorithm.

For that purpose, we define independent and dependent model parameters. We choose four independent parameters that are used to determine all other parameters, namely (1) melt density times gravitational acceleration, $\rho_m g = 1$ [Pa $\cdot$ m^{-1}], (2) permeability divided by melt viscosity, $\frac{k}{\eta_m} = 1$ [m^2 $\cdot$ Pa^{-1} $\cdot$ s^{-1}], (3) solid volumetric viscosity, $\eta_v = 1$ [Pa $\cdot$ s] and (4) temperature, $T^A = 1$ [K]. Next, we specify the following characteristic scales of the model: the characteristic length, $L_c = \sqrt{\frac{k}{\eta_m} \cdot \eta_v} = 1$ [m], the characteristic time, $t_c = \frac{\eta_v}{\rho_m g \cdot L_c} = 1$ [s], the characteristic stress, $P_c = \rho_m g \cdot L_c = 1$ [Pa], the characteristic power, $E_c = \frac{\rho_m g \cdot {L_c}^4}{t_c} = 1$ [W], the characteristic thermal conductivity, $\lambda_c = \frac{E_c}{L_c \cdot T^A} = 1$ [W $\cdot$ K^{-1} $\cdot$ m^{-1}], and the characteristic density times specific heat, $\mathrm{Cp}_c = \frac{\rho_m g \cdot L_c}{T^A} = 1$ [Pa $\cdot$ K^{-1}]. The characteristic length L_c of the model, also known as compaction length in the context of porosity waves (e.g. McKenzie 1985; Connolly & Podladchikov 2007), corresponds to the characteristic distance over which deformation occurs. Next, we define several dimensionally dependent scales to configure the model. These scales must be chosen in such way that the considered process can be numerically resolved and that the applied parameters are applicable to the considered process. Therefore, we apply a model height $Lx = 100 \cdot L_c$ and a width of perturbations in the initial distribution of porosity and/or total concentration of SiO_2, $w = 10 \cdot L_c$ so that the characteristic compaction for the two-phase flow can occur within the model domain and is affected by the size of initial perturbations. Furthermore, the solid density times gravitational acceleration $\rho_s g = \frac{\rho_{s,0}}{\rho_{m,0}} \cdot \rho_m g = 0.9423 \cdot \rho_m g$, which is a relation calculated for the reference point in the olivine system (see Fig. 3a and d). The shear viscosity is considered equal to the compaction viscosity $\eta_s = \eta_v = 1$. The thermal conductivity of melt and solid $\lambda_m = \lambda_s = 483 \cdot \lambda_c =$, which applies to a natural conductivity of 3 [W $\cdot$ m^{-1} $\cdot$ K^{-1}] if we assume a natural $L_c = 1$ km, $\eta_v = 1.25{\times}10^{20}$ Pas and $T^A = 1860$ [K] and reference melt density (Table 2). Similarly, the product of density times specific heat for melt and solid can be determined with reference values in Table 2 as $\mathrm{Cp}_m = 205 \cdot \mathrm{Cp}_c = 205$ and $\mathrm{Cp}_s = \frac{\rho_{s,0}}{\rho_{m,0}} \cdot \frac{\mathrm{Cp}_{s,0}}{\mathrm{Cp}_{m,0}} \cdot \mathrm{Cp}_m = 0.9014 \cdot \mathrm{Cp}_m = 184.7906 \cdot \mathrm{Cp}_c$.

To further configure the model, we define four initial profiles, namely for temperature, porosity, total silica mass fraction and total pressure (Fig. 5). First, we apply a constant porosity profile with a value of 0.02 and a constant total silica mass fraction profile with a value of 0.45 (in Fig. 4 this silica mass fraction corresponds to the grey dashed lines in the region where melt density is lower than solid density). We then add a perturbation to the porosity and/or the total silica mass fraction profiles in the form of a Gaussian with its maximum at a depth of $x = -20$ (Fig. 5g and h). For the simulations presented below, we apply five perturbation amplitudes for porosity, Δ (0.005, 0.01, 0.02, 0.03 and 0.04) and five for total silica mass fraction $\Delta C_T^{SiO_2}$ (0, 0.25, 0.5, 0.75 and 1; see Fig.6 for the systematic scheme of simulations). We define the temperature profile in the model with a temperature difference $\Delta T_{\mathrm{model}}$ of 2 between the

bottom and the top of our model (Fig. 5d). For the initial pressure profile, we calculate the lithostatic pressure across the model with the model total densities and obtain a pressure difference ΔP_{model} of approximately 90 for all simulations. We performed two series of systematic simulations with two different thermal gradients, one representing an adiabatic and one a conductive gradient. In order to adapt our temperature and pressure profiles in the model to realistic natural profiles, we must rescale the α and β parameters with a temperature ratio ($\Delta T_{\text{nature}}/\Delta T_{\text{model}}$) and a pressure ratio ($\Delta P_{\text{nature}}/\Delta P_{\text{model}}$). ΔT_{nature} is different depending on whether it represents an adiabatic or conductive gradient. We apply a natural pressure variation, ΔP_{nature}, across our model equal to 1 [GPa], which corresponds to the pressure range chosen for the thermodynamic data (Figs 2 and 3). Thus, we can determine a certain model height ($h = \frac{P}{\rho_T g}$, with $\rho_T = \rho_{m,0}\varphi + \rho_{s,0}(1-\varphi)$ and $\varphi = 0.02$) that we can use to calculate a natural temperature difference, $\Delta T_{nature,1}$, corresponding to a realistic adiabatic gradient. We found h~28 [km] and $\Delta T_{nature,1}$~15 [K] for an adiabatic gradient between 0.5-0.55 [$°C \cdot km^{-1}$]. To define the second, larger natural temperature difference $\Delta T_{nature,2}$ representing a conductive gradient at the base of the lithosphere, we multiplied $\Delta T_{nature,1}$ by ten, thus $\Delta T_{nature,2}$=150 [K].

3 Results

We first present results from the thermodynamic model which consist essentially of the determined values of α, β and γ for the thermodynamic variables (Table 2). Subsequently, we show results from the THMC melt migration model.

3.1 Linearization of thermodynamic results

The parameters α, β and γ are used to linearize the dependency of the thermodynamic variables on temperature, pressure and total silica content. For example, for the melt density the linearized relation is

$$\rho_m = \rho_{m,0} + \alpha_{\rho_m} T + \beta_{\rho_m} P + \gamma_{\rho_m} C_T^{\text{SiO}_2} \quad (18)$$

The calculated values of all α, β and γ are presented in Table 2. If values of α, β or γ are positive, then the corresponding parameter will increase with the respective increase of temperature, pressure or total silica mass fraction (e.g. in Fig. 3, ρ_m increase with increasing pressure, since β_{ρ_m} is positive). Consequently, if values α, β or γ are negative, then the associated parameter will decrease with the respective increasing temperature, pressure or total silica mass fraction (e.g. in Fig. 3, ρ_m decrease with increasing temperature, α_{ρ_m} is negative). The determined values of α, β and γ provide a transparent overview on the relative importance and interdependence of the parameters. For example, the α for solid density α_{ρ_s} and for solid mass fraction of silica $\alpha_{C_s^{\text{SiO}_2}}$ are 2 to 5 times larger than values of α for melt density α_{ρ_m} and for melt mass fraction of

silica $\alpha_{C_m^{\mathrm{SiO_2}}}$. This relationship is opposite for magnesium mass fraction where α for the melt, $\alpha_{C_m^{\mathrm{MgO}}}$, is 1.5 times larger than the solid one, $\alpha_{C_s^{\mathrm{Mgo}}}$. We observe the same trend for β, where β_{ρ_s} and $\beta_{C_s^{\mathrm{SiO_2}}}$ are 1.5 to 4 times larger than β_{ρ_m} and $\beta_{C_m^{\mathrm{SiO_2}}}$ and $\beta_{C_m^{\mathrm{Mgo}}}$ is slightly larger than $\beta_{C_s^{\mathrm{Mgo}}}$. For the γ the situation is different, because all γ values for melt (γ_{ρ_m}, $\gamma_{C_m^{\mathrm{Mgo}}}$ and $\gamma_{C_m^{\mathrm{SiO_2}}}$) are 2.5 to 4.5 times larger than γ values for solid (γ_{ρ_s}, $\gamma_{C_s^{\mathrm{Mgo}}}$ and $\gamma_{C_s^{\mathrm{SiO_2}}}$). This difference in dependence on P, T and $C_T^{\mathrm{SiO_2}}$ between variables related to melt and solid is between a factor of 1.5 and 4.5 and it is, hence, important to consider this difference in the THMC model.

We use the linearized relations employing parameters α, β and γ, instead of the results obtained directly from the Gibbs free energy minimization (Fig. 2), mainly because of computational efficiency, since direct usage of Gibbs energy minimisation results would require numerical interpolations in order to calculate the thermodynamic variables used in the THMC model. Such data interpolations are computationally time consuming, especially if the algorithm is extended to 2D (see below) or 3D.

Table 2. Values for linear approximation of thermodynamic variables. Values are calculated from Gibbs free energy minimisation and the experiment of Davis et al. (2011), see section 2.1 for details.

Adopted values for linearization:					
P_0	3.0001 10^9	[Pa]			
T_0	1863.15	[K]			
$C_{T,0}^{\mathrm{SiO_2}}$	0.3280	[ ]			
Value at reference point	alpha [K^{-1}]	beta [Pa^{-1}]	gamma [ ]		
$\rho_{m,0}$	$3.8631 \cdot 10^3$ [kg m^{-3}]	α_{ρ_m}	$-3.3260 \cdot 10^{-4}$	β_{ρ_m}	$3.2666 \cdot 10$
$\rho_{s,0}$	$3.6401 \cdot 10^3$ [kg m^{-3}]	α_{ρ_s}	$-6.5732 \cdot 10^{-4}$	β_{ρ_s}	$4.7575 \cdot 10$
$C_{m,0}^{\mathrm{MgO}}$	0.0449 [ ]	$\alpha_{C_m^{\mathrm{MgO}}}$	0.0073	$\beta_{C_m^{\mathrm{MgO}}}$	$-3.3051 \cdot 1$
$C_{s,0}^{\mathrm{MgO}}$	0.2232 [ ]	$\alpha_{C_s^{\mathrm{MgO}}}$	0.0047	$\beta_{C_s^{\mathrm{MgO}}}$	$-2.9722 \cdot 1$
$C_{m,0}^{\mathrm{SiO_2}}$	0.3079 [ ]	$\alpha_{C_m^{\mathrm{SiO_2}}}$	$2.3932 \cdot 10^{-4}$	$\beta_{C_m^{\mathrm{SiO_2}}}$	$-1.0870 \cdot 1$
$C_{s,0}^{\mathrm{SiO_2}}$	0.3481 [ ]	$\alpha_{C_s^{\mathrm{SiO_2}}}$	$6.8708 \cdot 10^{-4}$	$\beta_{C_s^{\mathrm{SiO_2}}}$	$-4.3008 \cdot 1$
$c_{p_{m,0}}$	$1.2481 \cdot 10^3$ [J kg^{-1} K^{-1}]				
$c_{p_{s,0}}$	$1.1940 \cdot 10^3$ [J kg^{-1} K^{-1}]				

The initial density profile of the model impacts the melt migration. For a constant chemical composition, the initial density profile is controlled by the initial variation of P and T, but with opposite trend: from the top to the bottom of the model, the melt and solid densities increase with increasing pressure but decrease with increasing temperature. We determine for the applied values of T and P the critical value of T, for which the density is constant with depth. We use the equation

$$\rho = \rho_0 + \alpha\, T + \beta\, P \quad (19)$$

and reformulate the equation to

$$\frac{\rho}{\alpha} = T + \frac{\beta}{\alpha}\, P \quad (20)$$

where $\rho = \rho - \rho_0$. We assume no density variation (isochoric system) with a variation of T and P, i.e. $\frac{\rho}{\alpha} = 0$ and solve the remaining equation for T which yields

$$T = -\frac{\beta}{\alpha}\, P \quad (21)$$

If the applied T is larger than the above expression, then the density is decreasing with depth in the model (i.e. the initial density variation is controlled by the temperature variation) and if T is smaller, then the density increases with depth, controlled by the pressure variation. The above analysis can also be applied to the mass fractions. Choosing P of 1 [GPa] and using α and β values from Table 2, we obtain for the melt density a critical T=98.2 [K], for the solid density a critical T=72.5 [K], for magnesium melt mass fraction a critical T=45.3 [K], for magnesium solid mass fraction a critical T=63.2 [K], for silica melt mass fraction a critical T=45.6 [K] and for silica solid mass fraction a critical T=62.6 [K]. All values of critical T are between $\Delta T_{nature,1}$ and $\Delta T_{nature,2}$, respectively, that is the temperature differences applied for the adiabatic and the conductive gradient. Therefore, the applied initial adiabatic and conductive geotherms cause a fundamentally different initial variation of densities and mass fractions with depth.

3.2 THMC model results: comparison of initial profiles, maximum melt velocity and evolution over time

We performed 50 simulations with one time step only to determine the initial profiles of all the involved model variables, because the initial profiles of, for example, the solid and melt velocities represent already an interesting result that needs to be calculated iteratively due to the nonlinear coupling of the model variables. For four of these simulations we also calculate the evolution with time to investigate the upward melt migration by reactive porosity waves.

Comparison of initial profiles We first compare initial profiles from four different simulations, namely simulations termed S05 with an initial porosity perturbation only and simulations S15 with an initial porosity and total silica mass fraction perturbations, both for the two temperature gradients, namely a

conductive gradient (Figs 5 and B12) and an adiabatic gradient (Figs B13 and B14). The four simulations show similar profiles for melt and total pressure (Fig. 5a), effective pressure, $P_e = P_m - P_T$ (Fig. 5c), temperature (Fig. 5d), porosity (Fig. 5g) and solid velocity (Fig. 5i). The effective pressure shows which part of the model is in compression (P_e is negative) and which part is in dilation (P_e is positive). The main difference between the four simulations is the maximum magnitudes of the peaks of corresponding profiles. Maximum magnitudes are larger in the two S15 simulations (Figs 5 and B14), with an initial perturbation in porosity and in total silica mass fraction, than in the two S05 simulations (Figs B12 and B13), with an initial perturbation only in porosity. Differences between the four simulations are visible in the calculated profiles of densities (Fig. 5b), of magnesium and silica mass fractions (Figs. 5e and h) and of melt velocity (Fig. 5f). There is a significant difference between simulations with a conductive gradient (Figs 5 and B12) and simulations with an adiabatic gradient (Figs B13 and B14). Across the model, density profiles for the conductive gradient (panel b in Figs. 5 and B12) decrease with increasing depth, whereas for the adiabatic gradient (panel b in Figs. B13 and B14), densities increase with increasing depth. This trend is reversed for melt and solid mass fraction of magnesium and silica (panels e and h in Figs 5, B12-14). For the conductive gradient, melt and solid mass fraction of magnesium and silica increase with increasing depth and with the adiabatic gradient, melt and solid mass fraction of magnesium and silica decrease with increasing depth. The calculated total magnesium mass fraction (black line in panel e in Fig. 5 and B12-14) follows the trend of melt and solid mass fractions of magnesium. The calculated total silica mass fraction (black line in panel h in Fig. 5 and B12-14) remains constant except in the region of the perturbation where the maximum value changes according to the applied initial perturbations. The melt velocity profiles (panel f in Fig. 5 and B12-14) exhibit the maximum melt velocity at the position where the maximum initial perturbation in porosity and/or total silica mass fraction is applied. The maximum melt velocity is greater when both porosity and total silica mass fraction profiles exhibit initial perturbations (simulation S15, Figs 5 and B14). A difference also exist in the overall slope of the melt velocity profiles between the two different temperature gradients in all four simulations. The melt velocity decreases with depth for the conductive gradient (Figs 5 and B12) and increases with depth for the adiabatic gradient (Figs B13 and B14). The initial melt velocity profile shows positive values indicating upward motion of the melt (Figs 5, B12-14 panel e). In the region where the initial perturbation in porosity and silica mass fraction is applied the melt velocity is largest. In this region, the solid velocity is negative indicating compaction in the region where the melt is moving upward, or where melt is extracted (Figs 5, B12-14 panel i). Also, the absolute magnitudes of the melt velocities around the maximal initial perturbation are approximately one order of magnitude larger than absolute magnitudes of the solid velocities.

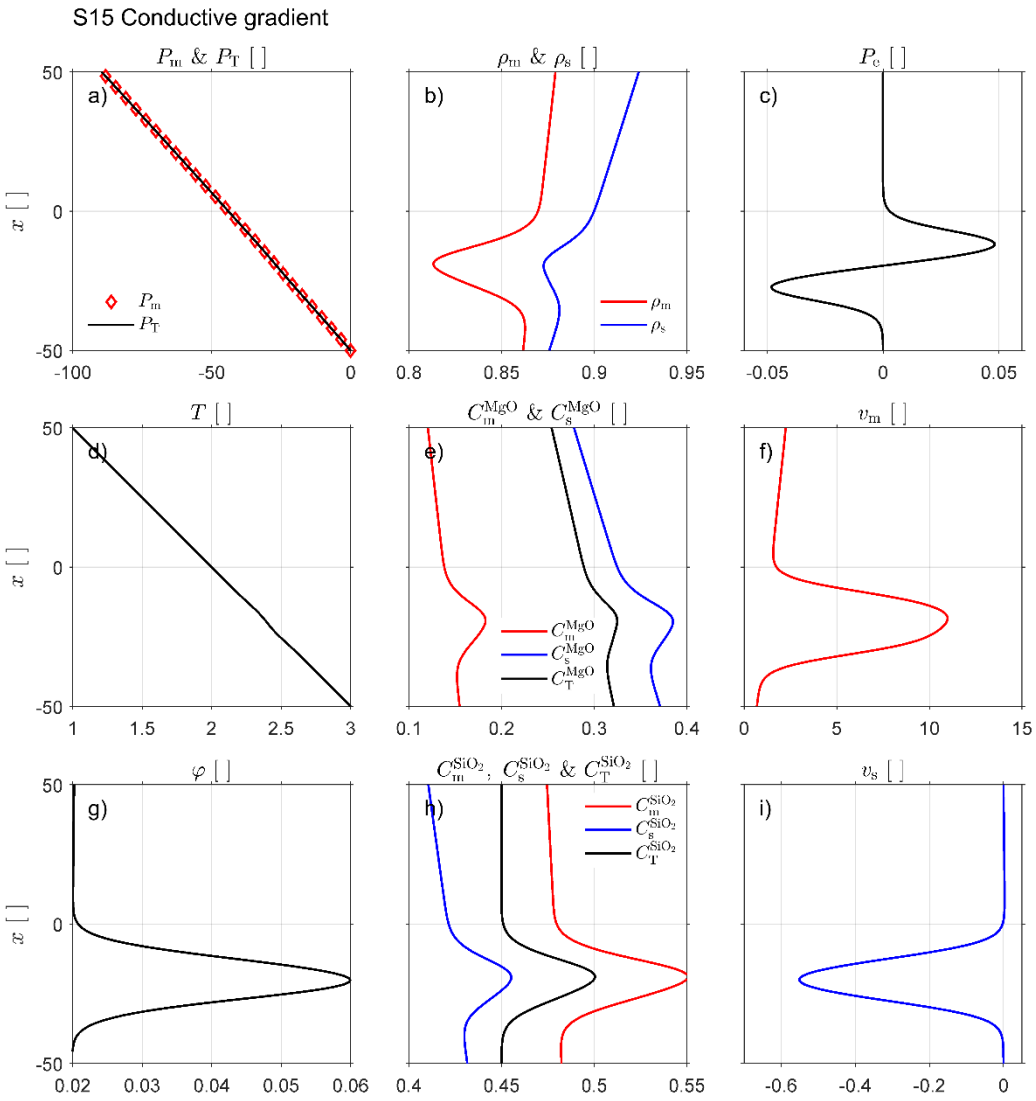

Figure 5. Initial profiles of simulation S15 for a conductive gradient. All variables are dimensionless. Panel (a) shows melt pressure (red diamond) and total pressure (black line). Panel (b) shows melt density (red line) and solid density (blue line). Panel (c) shows effective pressure, positive values indicate decompaction while negative values indicate compaction. Panel (d) shows temperature. Panel (e) shows magnesium mass fraction in melt (red line) and in solid (blue line) and total magnesium mass fraction (black line). Panel (f) shows melt velocity. Panel (g) shows porosity. Panel (h) shows silica mass fraction in melt (red line) and in the solid (blue line) and total silica mass fraction (black line).

Panel (i) shows solid velocity.

Comparison of maximum melt velocity Figure 6 compares maximum melt velocities of the respective initial profiles for 50 simulations. We made 25 simulations with an adiabatic gradient (Fig. 6a) and 25 simulations with a conductive gradient (Fig. 6b). For each thermal gradient, we applied 5 perturbation amplitudes for the initial porosity, Δ , and 5 amplitudes for the initial total silica mass fraction, $\Delta C_T^{\mathrm{SiO_2}}$. The four simulations selected for investigating the time evolution, i.e. S05 and S15, are represented by the points circled in red (Fig. 6). The greater the amplitudes of the perturbations, the greater the maximum melt velocity. The maximum melt velocity occurs when both perturbation amplitudes are maximal, which applies for both thermal gradients. The maximal melt velocities are slightly larger for an adiabatic gradient (Fig. 6). The curved velocity contours in figure 6 indicate a nonlinear dependence between the maximal melt velocity and Δ and $\Delta C_T^{\mathrm{SiO_2}}$. However, the 25 maximal melt velocities for each thermal gradient can be collapsed from the two dimensional space (Δ - $\Delta C_T^{\mathrm{SiO_2}}$) onto a one dimensional space (Fig. 6c and d). The equations of this data collapse are obtained by a linear best fit of the 25 data points and are given as label of the horizontal axis. The two best-fit equations show that the difference in maximal melt velocity for the two thermal gradients is only due to a different sensitivity to $\Delta C_T^{\mathrm{SiO_2}}$, with exponents 1.1 and 1.2, because the exponents of Δ are identical for the two thermal gradients (Fig. 6c and d). Overall, for the chosen parameters, a perturbation in total silica mass fraction has a similar impact on the maximal melt velocity as a perturbation in the initial porosity.

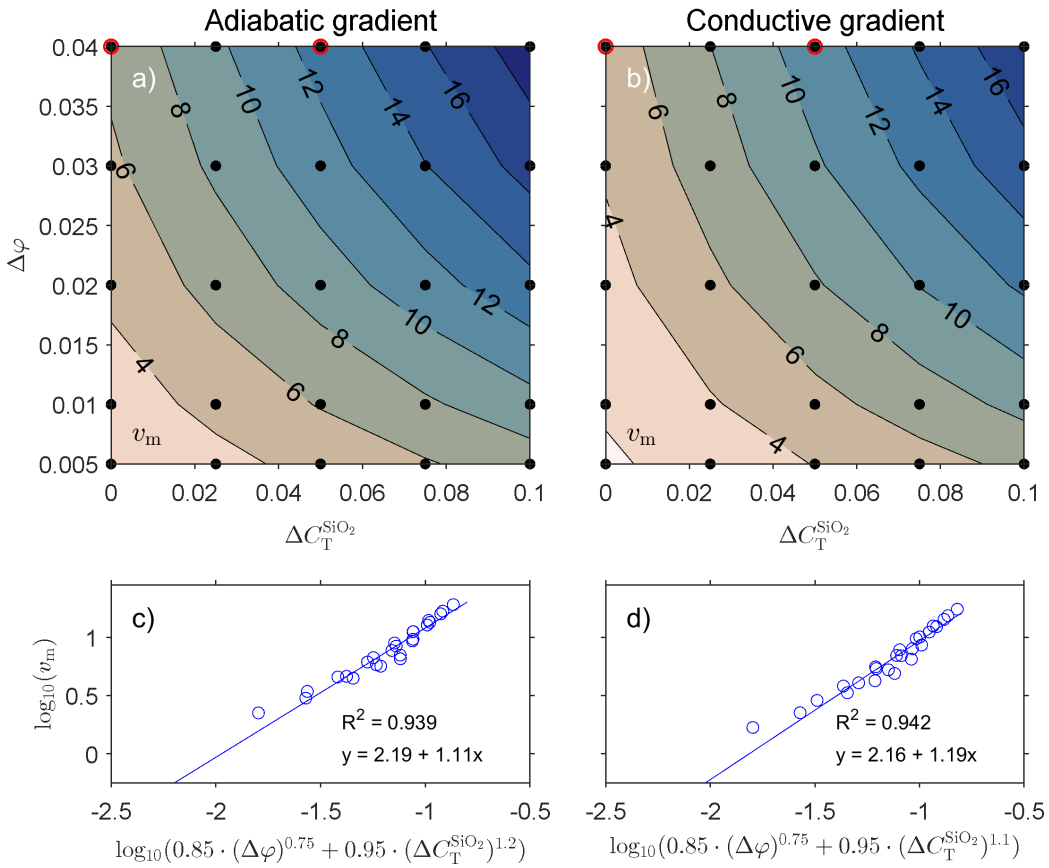

Figure 6. Panels (a) and (b) show maximal initial melt velocities as function of initial porosity, Δ , and total silica mass fraction, $\Delta C_T^{SiO_2}$, perturbation amplitudes. (a) for adiabatic gradient and (b) for conductive gradient. Black lines show the velocity contours and red circles indicate the initial perturbations for four simulations for which the time evolution has been calculated; respectively simulations S05 (top left in panels a and b) and S15 (top in the middle in panels a and b) for both temperature gradients. Panels (c) and (d) show the power low relationship between melt velocity and a combination of porosity and total silica mass fraction perturbation amplitude, (c) for adiabatic gradient and (d) for conductive gradient. In each panel, blue points represent the 25 systematic simulations and the blue line the linear regression line.

Time evolution and reactive porosity wave propagation Figure 7 shows the time evolution of the S15 simulation with a conductive gradient. The additional figures B15 to B17 show the three other simulations, namely S05 with a conductive gradient, and S05 and S15 with an adiabatic gradient. The evolution of porosity (Fig. 7a) and of effective pressure (Fig. 7b) corresponds to the typi-

cal evolution of 1D porosity waves (e.g. Connolly & Podladchikov 2013; Jordan et al. 2018). During porosity wave propagation, the maximum porosity always corresponds to an effective pressure of zero (Fig. 7a and b). The compaction at the base of the high porosity region (where P_e is minimum) allows the melt to rise upward into the high porosity region under decompaction (where P_e is maximum). Comparing all porosity profiles (panel a in Fig. 7 and B15-B17), for the two S05 simulations (Figs B15 and B16), the maximum porosity decreases slightly with progressive time and then remains constant, whereas for the two S15 simulations (Figs 7 and B17), the maximum porosity increases and then decreases slightly. The two simulations with an adiabatic gradient (Figs B16 for S05 and B17 for S15) show a stabilisation of the maximum melt velocity over time, while the two simulations with a conductive gradient (Figs B15 for S05 and 7 for S15) show a slight increase in melt velocity over time. For the four simulations (Figs 7 and B15-B17), the variations of melt density and total silica mass fraction are small over time compared to the total magnesium mass fraction which show a slightly greater variation, especially for simulations with an adiabatic gradient (Figs B16 and B17).

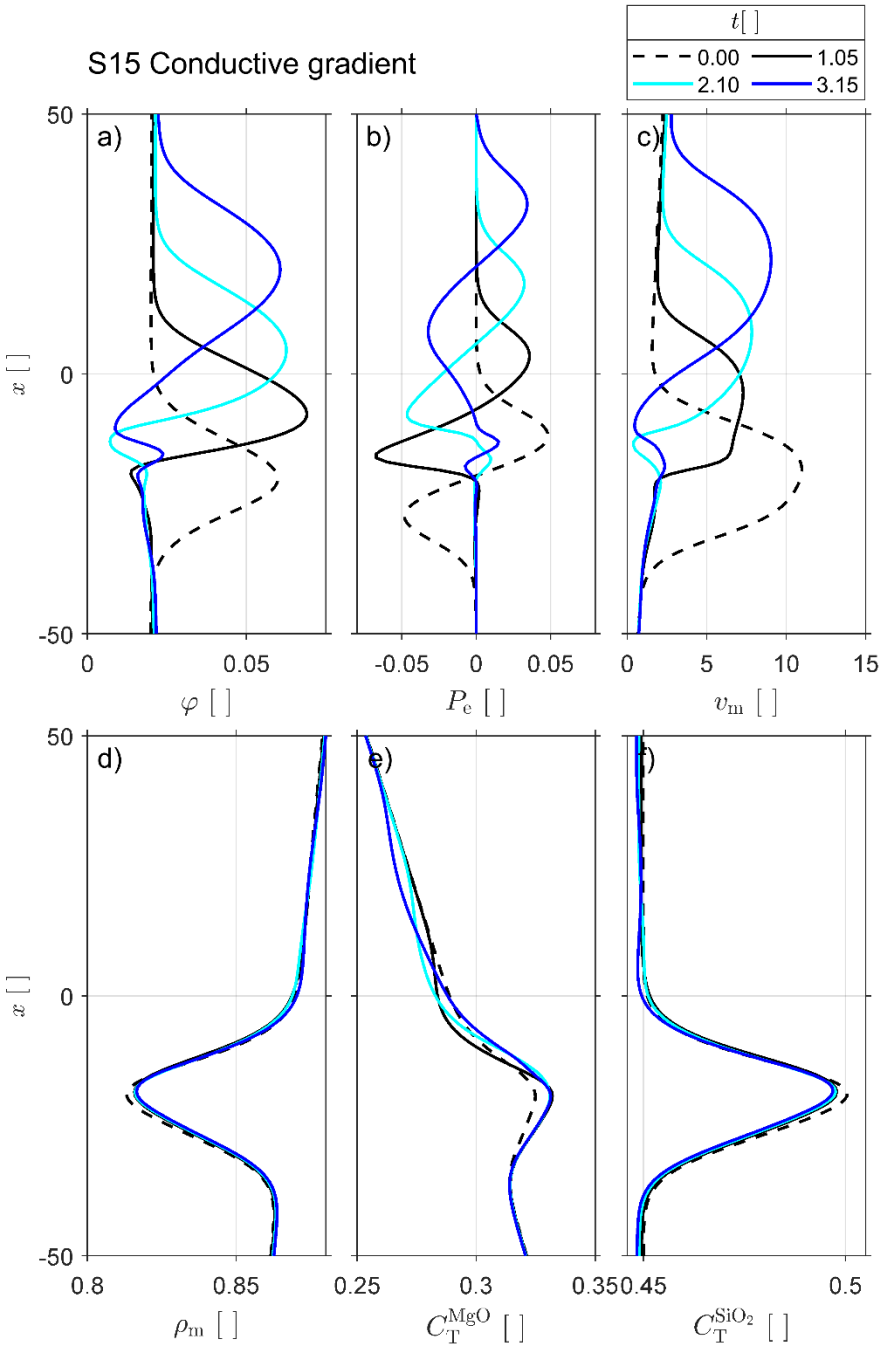

Figure 7. Time evolution of six variables in simulation S15 Conductive gradient; all variables are dimensionless. Panel (a) shows porosity, panel (b) shows effec-

tive pressure, panel (c) shows melt velocity, panel (d) shows melt density, panel (e) shows total magnesium mass fraction and panel (f) shows total silica mass fraction. Four time steps are chosen at different dimensional times: t = 0 with dashed line (corresponding to the initial profiles in figure 5 for each variables), t = 1.05 with black line, t = 2.10 with light blue and t = 3.15 with dark blue (see legend).

Figure 8 shows the time evolution of the melt density (panel a), the total magnesium mass fraction (panel b) and the total silica mass fraction (panel c) at depth $x = 10$ [ ] for the four simulations. The variation in melt density (Fig. 8a) for the two S05 simulations (conductive in light blue and adiabatic in grey) and the two S15 simulations (conductive in dark blue and adiabatic in black) is very similar. The main difference is the magnitude of the initial value at time $t = 0$ for the two different thermal gradients. The initial value for the conductive gradient is larger than the initial value for the adiabatic gradient (ρ_m of S05 and S15 conductive $> \rho_m$ of S05 and S15 adiabatic). Similar variations are observed for total magnesium mass fraction (panel b) for the two S05 simulations (conductive in light blue and adiabatic in grey) and the two S15 simulations (conductive in dark blue and adiabatic in black). For melt density, the magnitude of the initial value at time $t = 0$ between the two thermal gradients are different. The initial value for the adiabatic gradient is larger than the initial value for the conductive gradient (C_T^{MgO} of S05 and S15 adiabatic $> C_T^{\mathrm{MgO}}$ of S05 and S15 conductive). For the variation of the total silica mass fraction (panel c), the initial value is identical for all four simulations since this value is specified as initial condition. The local variation of the total silica mass fraction over time is larger than the initial value (at $t = 0$) for the simulations with an adiabatic gradient (black and grey lines) and is smaller for the simulations with a conductive gradient (dark and light blue lines). The maximum peaks of the two S15 simulations (black and dark blue lines) arrive before the maximum peaks of the two S05 simulations (grey and light blue lines). This is consistent with the fact that S15 simulations have a greater initial perturbation, hence the melt velocity is larger and the maximum peaks arrive first.

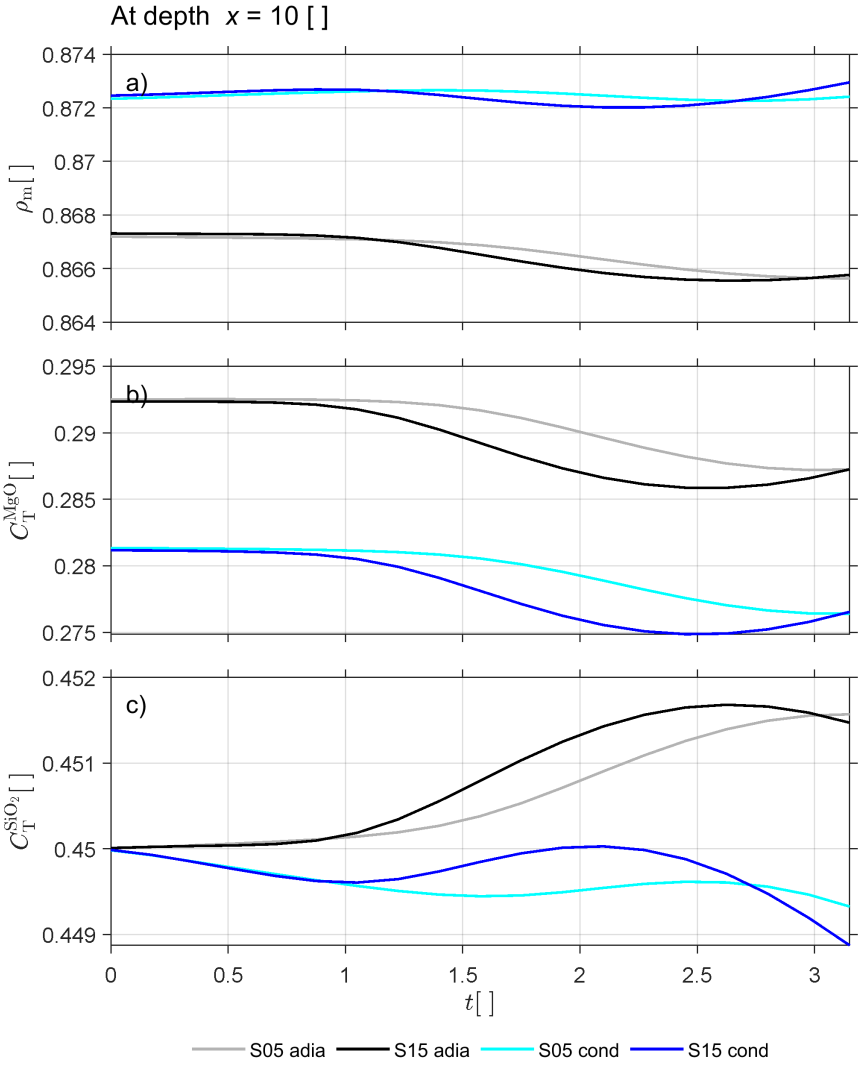

Figure 8. Time evolution, at a fixed depth of x = 10, of three variables for the four simulations indicated by red circles in figure 6: simulation S05 for adiabatic gradient in grey, simulation S15 for adiabatic gradient in black, simulation S05 for conductive gradient in light blue and simulation S15 for conductive gradient in dark blue. All variables are dimensionless. Panel (a) shows melt density. Panel (b) shows total magnesium mass fraction and panel (c) shows total silica mass fraction.

4 Discussion

4.1 Mobility and mass transport

In the modelled chemical system, the mass fractions of MgO and SiO_2 in the melt and solid are variable and are functions of pressure, temperature and total silica content. Our model can be considered as fully mobile since there are no restrictions on the mobility of MgO and SiO_2 so that MgO and SiO_2 can be freely exchanged between solid and melt. This full mobility is an elaboration compared to existing studies on reactive transport with fluid-rock interactions, who assume that some chemical components are immobile and fixed to the solid phase (e.g. Plümper et al. 2016, Beinlich et al., 2020). Furthermore, in our model the total mass of MgO and SiO_2 can locally change permanently due to mass transport by melt migration since the total mass of SiO_2 can locally change permanently. In contrast, other studies on melt migration with chemical differentiation consider the silica mass fraction as a function of temperature only (e.g. Jackson et al., 2018). Therefore, for a given temperature the silica mass fraction cannot change by transport. In our model, the mobility and mass transport are enabled by a freely evolving porosity, which is calculated from the conservation equation for the total mass of MgO. For example, inside the considered partial melting region of the olivine phase diagram (Fig. 1), the densities (Fig. 1b) and mass fractions of MgO of solid and melt (Fig.1c) are fixed for a given temperature and pressure, independent on the composition X (Gibbs phase rule). The total mass of MgO is calculated by the mass fractions, densities and porosity. If the total mass of MgO is locally modified due to an advective melt flux, and densities and mass fractions of MgO are fixed, then the porosity of the system must change to enable and balance the mass transport.

4.2 Magnesium in melt

For the applied simple chemistry, our thermodynamic model predicts an increase of the magnesium mass fraction in the melt, C_m^{MgO}, with increasing pressure (Figs. 5 and B12). Partial melting experiments of peridotite have shown also that the MgO mass fraction in the melt increases with pressure (Fig. 9). The black line in figure 9 represents the numerically modelled profile of C_m^{MgO} for a conductive thermal gradient (simulation S15). Therefore, despite the applied simplified chemistry for the mantle composition, the modelled gradient of C_m^{MgO} shows a similar trend than the experimental data. Our model shows smaller absolute values of C_m^{MgO} than the experiments, which is due to the applied simplified chemistry.

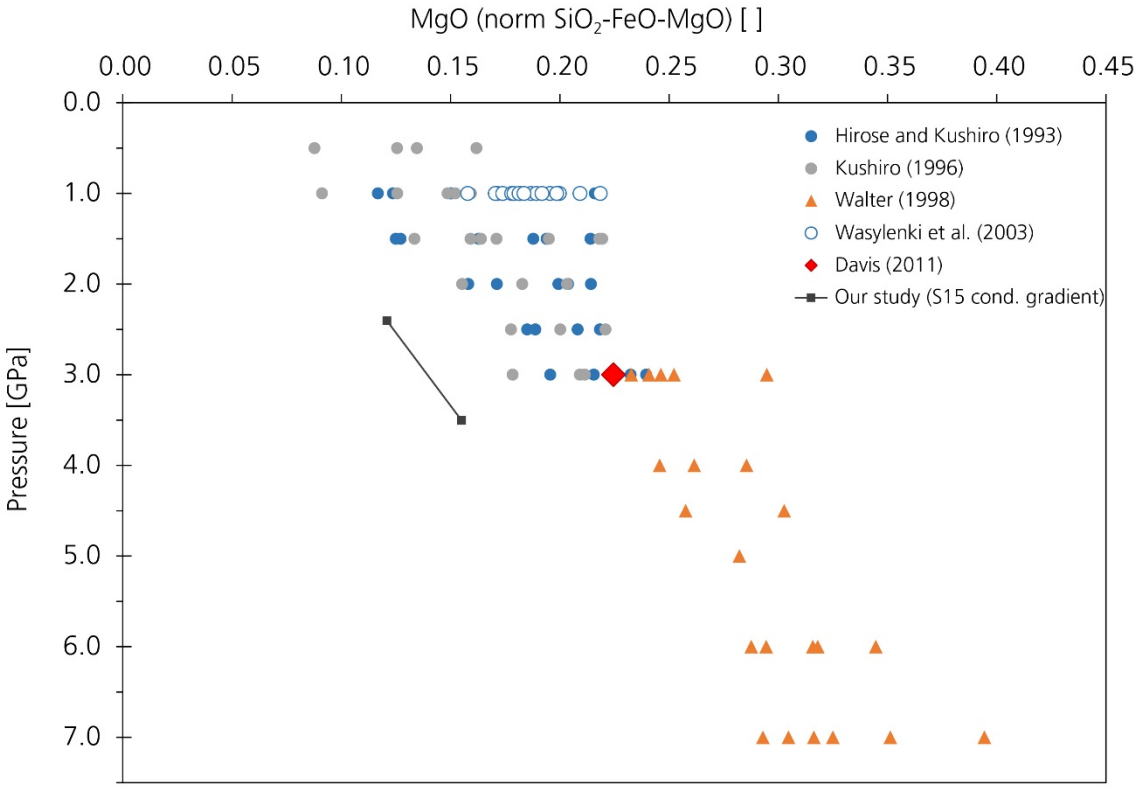

Figure 9. Magnesium melt mass fractions of five partial melting experiments of peridotite vs. pressure. Filled blue circles are data from Hirose & Kushiro (1993). Filled grey circles are data from Kushiro (1996). Filled orange triangles are data from Walter (1998). Filled white circles are data from Wasylenki et al. (2003). The filled red diamond is 0% melt from Davis et al. (2011). The horizontal evolution of MgO at each pressure correspond to the increase in partial melting rate. The black line shows the overall gradient of MgO mass fraction in the melt resulting from our study without the perturbation (corresponding to the C_m^{MgO} profile in Figure 5e).

4.3 2D reactive porosity wave model, channelization and melt-rock interaction

A characteristic feature of porosity wave propagation in 2D and 3D is the possibility to change the shape of the propagating wave, which can be either blob-like (Fig. 10 a-h) or channel-like (Fig. 10 i-p) (e.g. Connolly & Podladchikov, 2007; Räss et al., 2019). The shape of the propagating wave is controlled by the ratio of shear to bulk viscosity ($\frac{\eta_s}{\eta_v}$) and the ratio of decompaction to compaction bulk viscosity ($\frac{\eta_d}{\eta_v}$) (e.g. Räss et al., 2019). A value of $\frac{\eta_d}{\eta_v} < 1$ is termed decompaction weakening. If both viscosity ratios are equal to one, the propagation

is a blob-like for a circular initial perturbation in porosity. If decompaction weakening is significant, then the propagating porosity wave forms a channel (e.g. Connolly & Podladchikov, 2007; Räss et al., 2019). 2D and 3D models of porosity waves are important to study the mass transport of melt because the effective mass transport predicted by 1D models is less compared to predictions of 2D models (Jordan et al., 2018). The presented 1D THMC transport model is straightforward expandable to 2D and 3D. The main difference compared to the 1D model is that the deformation of the viscous solid must be calculated with a 2D model for viscous flow including both shear and normal deviatoric stresses. For all other conservation equations simply the 2D advective and diffusive fluxes must be added. We present here first results of two 2D models to show the localization of flow from a blob-like (Fig. 10 a-d) to a channel-like geometry (Fig. 10 i-l) and associated evolutions of the total silica content (Fig. 10 e-h and m-p). The 2D models employ mostly the same parameters as the 1D model, but, for example, the initial perturbation of the porosity has the form of a 2D Gaussian. For the model with blob-like geometry, we apply $\frac{\eta_s}{\eta_v} = 1$ and $\frac{\eta_d}{\eta_v} = 1$ and for the model with channel-like geometry $\frac{\eta_s}{\eta_v} = 25$ and $\frac{\eta_d}{\eta_v} = 0.1$.

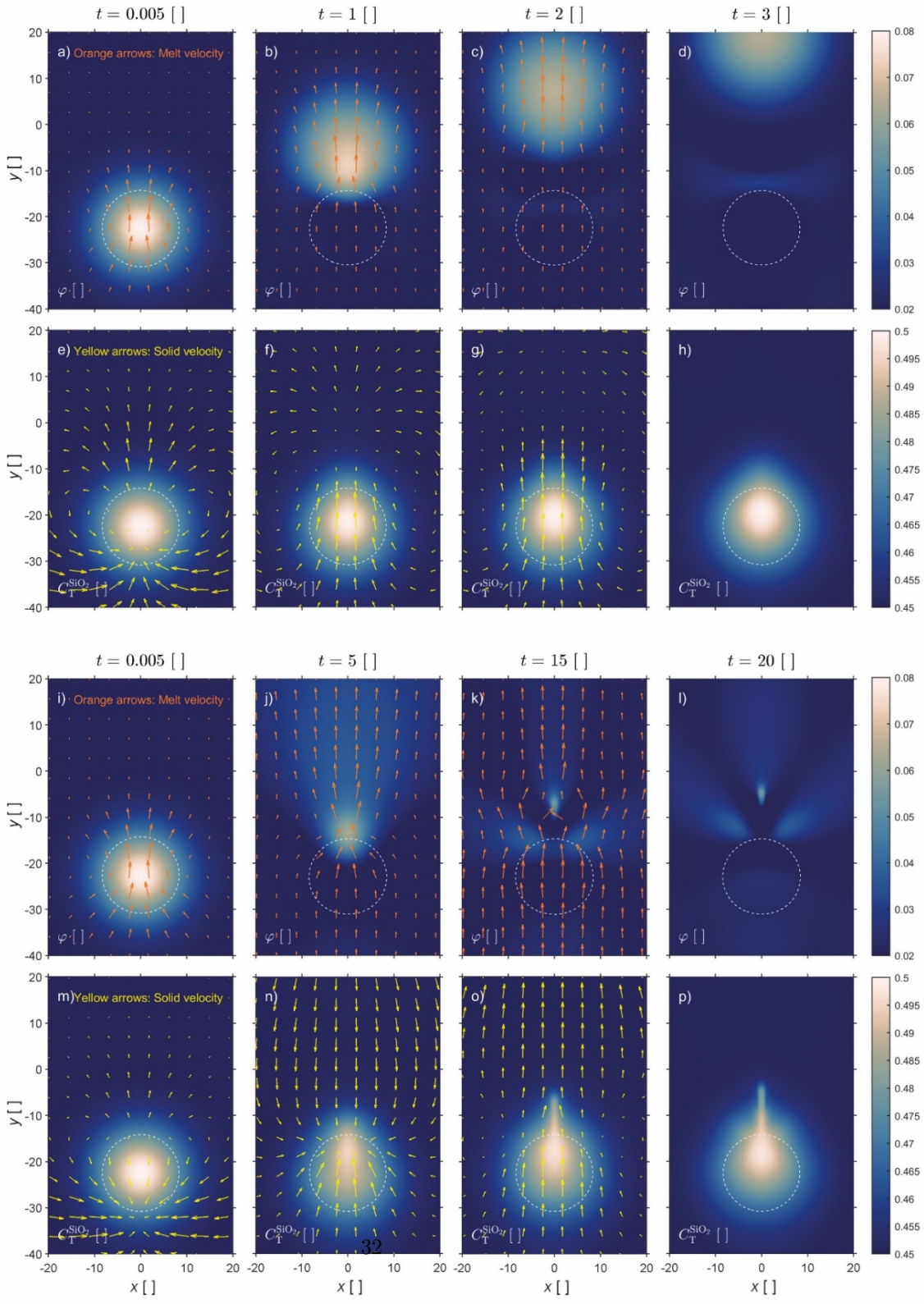
t = 0.005 [ ]
t = 1 [ ]
t = 2 [ ]
t = 3 [ ]
a) Orange arrows: Melt velocity
b)
c)
d)
e) Yellow arrows: Solid velocity
f)
g)
h)
t = 0.005 [ ]
t = 5 [ ]
t = 15 [ ]
t = 20 [ ]
i) Orange arrows: Melt velocity
j)
k)
l)
m) Yellow arrows: Solid velocity
n)
o)
p)
y [ ]
x [ ]
φ [ ]
$C_T^{SiO_2}$ [ ]

Figure 10. Time evolution of two 2D melt migration models by reactive porosity waves. Panels (a-d) show the porosity and panels (e-h) the total silica mass fraction for the blob-like simulation at four time steps (0.005, 1, 2 and 3). (η_s/η_v)= 1 and (η_d/η_v)= 1 for the blob-like simulation. Panels (i-l) show the porosity and panels (m-p) the total silica mass fraction for the channel-like simulation at four time steps (0.005, 5, 15 and 20). (η_s/η_v)= 25 and (η_d/η_v)= $\eta_v/100$= 0.1 for the channel-like simulation. Orange arrows show melt velocity, yellow arrows show solid velocity and dashed circles the position of initial perturbations. All variables are dimensionless.

Panels (d), (h), (l) and (p) in figure 10 show the chemical exchange between melt and solid in both simulations by the different evolution of the porosity and the total silica mass fraction. This exchange enables an enrichment of total silica in the solid and a differentiation of the melt in the pores.

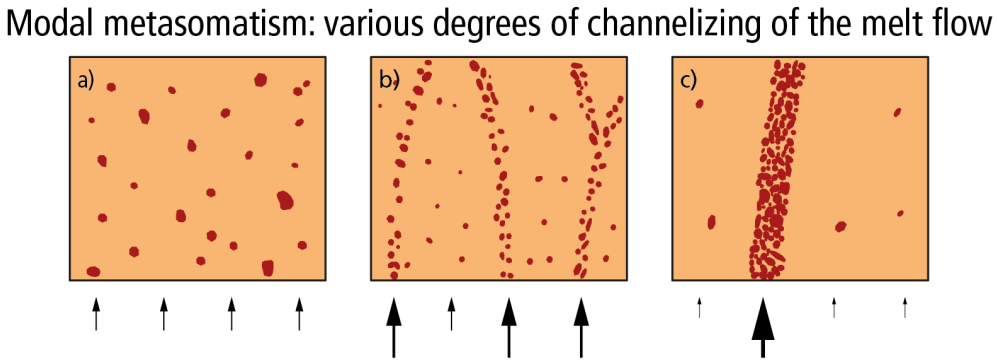

Figure 11. Schematic illustration showing the various degrees of channelizing of the melt flow in function of the distribution of melt flux. Redrawn form Harte et al. 1993.

The migration of melt by either blob-like or by channelized flow is an important process to consider for understanding metasomatism in a ductile region. Following the schematic illustration of Harte et al. (1993) (Fig. 11), the focusing of melt arriving in a rock to be eventually metasomatised (indicated by black arrows) has an impact on the type of metasomatism; from a pervasive metasomatism (Fig. 11a), through the formation of veins (Fig. 11b) to channels (Fig. 11c). Another important aspect is the melt-rock equilibration at every time step in the model. In the 2D simulation presented in figure 10, blob-like migration shows the importance of reaction as the chemical anomaly doesn't rise with the porosity but is accommodated by the solid via melt-rock reaction. This is illustrated by the comparison between the location of the porosity perturbation in figure 10d and the zone with higher total SiO_2 mass fraction, which is still close to the initial perturbation indicated by the dashed circle. In contrast, in the channel-like migration the porosity is focusing and allows the chemical perturbation to rise (Fig. 10l and p). The combination of melt-rock reaction with the type of melt migration seems therefore fundamental to understand the type

of metasomatism recorded in the lithospheric mantle.

An example of melt-rock reaction has been recently considered by Tomlinson & Kamber (2021) to explain the formation and evolution of the subcontinental cratonic lithospheric mantle. Xenoliths sampled by kimberlites have revealed that the cratonic lithosphere is heterogeneous and contains olivine with high magnesium content ($Fo92 - 94$), which requires extensive melting (Boyd & Mertzman, 1987; Herzberg, 1993). One interesting feature of this peridotitite xenolith suite is the lower MgO / SiO_2 ratio for a given magnesium number ($Mg\#$) of Archean subcontinental cratonic lithosphere regarding younger subcontinental lithospheric mantle. While various hypotheses have been proposed to explain this feature (e.g. Boyd & Mertzman, 1987; Herzberg, 1993), Tomlinson & Kamber (2021) suggest that silica enrichment in cratonic lithosphere could be associated to the migration of komatiite magma produced in episodic hot asthenospheric upwellings, which interact with previously depleted peridotite. Their melt-peridotite interaction is supported by THERMOCALC calculations, but no physical aspect on melt migration is considered. Although our thermodynamic calculation does not yet allow to predict natural melt-peridote chemical interactions due to our simplified chemical system, which does not take into account pyroxene crystallization or dissolution, the mechanical aspects of our model provide some new insights of melt-percolation within the ductile lithospheric mantle, supporting potential channelization of melt passing through a cratonic lithosphere.

4.4 Estimates of melt velocity

We can use the characteristic values of L_c and t_c to calculate a dimensional melt velocity from the numerically calculated melt velocity, by applying representative values for melt viscosity, volumetric viscosity and porosity. Using a porosity φ of 2%, the effective permeability is in the order of $k = 10^{-7} \cdot \varphi^3 = 8 \cdot 10^{-13}$ [m^2] (e.g. Connolly and Podladchikov, 2007). We assume values for melt viscosity η_m between 0.1 and 10 [$Pa \cdot s$] (e.g. McKenzie, 1989). We further assume that the volumetric viscosity η_v is identical to the shear viscosity around the LAB and use 10^{19} [$Pa \cdot s$], in agreement with numerical lithosphere subduction simulations of Bessat et al. (2020). The applied melt density is the reference density ($\rho_{m,0} = 3863$ [$kg\ m^{-3}$]). Taking a typical velocity of 12 from the two simulations S15 (red dots in the top middle in Fig. 6a and b), we obtain a dimensional melt velocity between 1 to 115 [$m \cdot yr^{-1}$]. Modifying the porosity φ to 1 and 0.5%, and the associated permeability, and using a melt viscosity $\eta_m$of 0.1 [$Pa \cdot s$], which seems more realistic for low degree melts rising in the lithosphere, we obtain velocities between 14.3 [$m \cdot yr^{-1}$] and 1.8 [$m \cdot yr^{-1}$] for a porosity of 1 and 0.5%, respectively. Using a larger melt viscosity $\eta_m$of 10 [$Pa \cdot s$], as used by Connolly et al. (2009) to estimate melt velocity at mid ocean ridges, we obtain 14 [$cm \cdot yr^{-1}$] and 1.8 [$cm \cdot yr^{-1}$], respectively. The melt velocities estimated above agree to first order with melt transport velocities deduced from centrifuge experiments by Connolly et al. (2009), which are 2 to 150 [$m \cdot yr^{-1}$] and considered applicable for melt rising at mid-ocean-ridges.

5 Conclusions

We present a new numerical model for two-phase melt migration in a deformable viscous solid coupled to chemical differentiation. The model is based on the coupling of a thermo-hydro-mechanical-chemical (THMC) transport model with thermodynamic results that have been precomputed by Gibbs energy minimization. For the considered system of forsterite-fayalite-silica, the solid and melt densities and the mass fractions of MgO and SiO_2 in both solid and melt are fully mobile, and all densities and mass fractions vary with temperature, pressure and total silica content. Therefore, the model is suitable to investigate chemical differentiation, metasomatism and melt-rock interaction during melt migration. The developed 1D and 2D THMC transport model can generate porosity waves. The initial variation of porosity and total silica content has a strong impact on the melt velocity. Also, the employed thermal gradient in the model, either adiabatic or conductive, has an impact on the melt velocity, and higher velocities result from an adiabatic gradient. For conditions applicable to the lithosphere-asthenosphere boundary, the densities for an adiabatic gradient generally increase with depth and increasing pressure, while for a conductive gradient the densities decrease with increasing depth. The thermal gradient, therefore, has a considerable impact on the vertical variation of solid and melt densities and mass fractions and, hence, on the chemical differentiation during melt migration. Application of a range of typical lithosphere values for porosity, permeability, melt and compaction viscosities provides reasonable melt velocities between 10 [$\mathrm{cm \cdot yr^{-1}}$] and 100 [$\mathrm{m \cdot yr^{-1}}$].

The preliminary 2D version of the model can generate blob-like and channel-like porosity waves. First 2D results show that the total silica mass transport is more efficient by channel-like porosity waves than by blob-like porosity waves, which has important implications for understanding metasomatism during melt migration across the ductile lithosphere.

The thermodynamic results show that the sensitivity of solid and melt densities to variations in P, T and $C_T^{SiO_2}$, expressed by the coefficients α, β and γ, can be considerably different. The same applies for the solid and melt mass fractions of MgO and SiO_2. Particularly, the sensitivity to chemical variations in $C_T^{SiO_2}$ is considerably different for the corresponding densities and considered mass fractions of the solid and melt phases. Hence, it is important to treat the dependencies of densities and mass fractions of solid and melt phase on variations in P, T and $C_T^{SiO_2}$ independently in a THMC melt migration model and to determine these dependencies with thermodynamic calculations.

Acknowledgements

Data Policy: For the review process, we add the input data and a working version of the 1D numerical code as supplementary material. The presented results can be generated with the input data and the 1D code. If the manuscript would be eventually accepted, then we would put the input data together with a documented version of the numerical 1D THMC transport code (written in

MATLAB) on the Zenodo server.

References

Aharonov, E., Whitehead, J. A., Kelemen, P. B., 1995. Channeling instability of upwelling melt in the mantle. *Journal of Geophysical Research*, **100(B10)**, 20433-20450.

Aharonov, E., Spiegelman, M., Kelemen, P. B., 1997. Three-dimensional flow and reaction in porous media: Implications for the earth's mantle and sedimentary basins. *Journal of Geophysical Research: Solid Earth*, **102(B7)**, 14821-14833.

Ahern, J., Turcotte, D., 1979. Magma migration beneath an ocean ridge. *Earth and Planetary Science Letters*, **45(1)**, 115-122.

Beinlich, A. J. T., Vrijmoed, J. C., Tominaga, M. M. T., Podladchikov, Y. Y., 2020. Instantaneous rock transformations in the deep crust driven by reactive fluid flow. *Nature Geoscience*, **13(4)**, 307-311.

Bessat, A., Duretz, T., Hetényi, G., Pilet, S., Schmalholz, S. M., 2020. Stress and deformation mechanisms at a subduction zone: insights from 2-d thermomechanical numerical modelling. *Geophysical Journal International*, **221(3)**, 1605-1625.

Best, M., 1974. Mantle-derived amphibole within inclusions in alkalic-basaltic lavas. *Journal of Geophysical Research*, **79(14)**, 2107-2113.

Boyd, F., Mertzman, S., 1987. Composition and structure of the kaapvaal lithosphere, southern africa. *Magmatic processes: physicochemical principles*, **1**, 3-12.

Burov, E. B., 2011. Rheology and strength of the lithosphere. *Marine and Petroleum Geology*, **28(8)**, 1402-1443.

Chakraborty, S., 2017. A new mechanism for upper crustal fluid flow driven by solitary porosity waves in rigid reactive media?. *Geophysical Research Letters*, **44(20)**, 10324-10327.

Connolly, J. A. D., Podladchikov, Y. Y., 1998. Compaction-driven fluid flow in viscoelastic rock. *Geodinamica Acta*, **11(2-3)**, 55-84.

Connolly, J. A. D., Podladchikov, Y. Y., 2007. Decompaction weakening and channeling instability in ductile porous media: Implications for asthenospheric melt segregation. *Journal of Geophysical Research*, **112(B10)**.

Connolly, J. A. D., Podladchikov, Y. Y., 2013. A hydromechanical model for lower crustal fluid flow. In: *Metasomatism and the chemical transformation of Rock*, pp. 599-658. Springer, Berlin, Heidelberg.

Connolly, J. A. D., Schmidt, M. W., Solferino, G., Bagdassarov, N., 2009. Permeability of asthenospheric mantle and melt extraction rates at mid-ocean

ridges. *Nature*, **462(7270)**, 209-212.

Cruden, A. R., 1988. Deformation around a rising diapir modeled by creeping flow past a sphere. *Tectonics*, **7(5)**, 1091-1101.

Davis, F., Hirschmann, M., Humayun, M., 2011. The composition of the incipient partial melt of garnet peridotite at 3GPa and the origin of OIB. *Earth and Planetary Science Letters*, **308(3-4)**, 380-390.

Duretz, T., Räss, L., Podladchikov, Y., Schmalholz, S., 2019. Resolving thermomechanical coupling in two and three dimensions: spontaneous strain localization owing to shear heating. *Geophysical Journal International*, **216(1)**, 365-379.

Francis, D., 1976. The origin of amphibole in lherzolite xenoliths from nunivak island, alaska. *Journal of Petrology*, **17(3)**, 357-378.

Gerya, T., 2019. Introduction to Numerical Geodynamic Modelling, 2nd Edition. Cambridge University Press, Cambridge.

Griffin, W., O'reilly, S. Y., Afonso, J. C., Begg, G., 2009. The composition and evolution of lithospheric mantle: a re-evaluation and its tectonic implications. *Journal of Petrology*, **50(7)**, 1185-1204.

Harte, B., Hunter, R., Kinny, P., 1993. Melt geometry, movement and crystallization, in relation to mantle dykes, veins and metasomatism. *Philosophical Transactions of the Royal Society of London. Series A: Physical and Engineering Sciences*, **342(1663)**, 1-21.

Herzberg, C. T., Baker, M. B., Wendlandt, R. F., 1982. Olivine flotation and settling experiments on the join Mg2SiO4-Fe2SiO2. *Contributions to Mineralogy and Petrology*, **80(4),** 319-323.

Herzberg, C. T., 1993. Lithosphere peridotites of the Kaapvaal craton. *Earth and Planetary Science Letters*, **120(1-2)**, 13-29.

Hirose, K., Kushiro, I., 1993. Partial melting of dry peridotites at high pressures: Determination of compositions of melts segregated from peridotite using aggregates of diamond. *Earth and Planetary Science Letters*, **114(4)**, 477-489.

Hofmann, A., 1972. Chromatographic theory of infiltration metasomatism and its application to feldspars. *American Journal of Science*, **272(1)**, 69-90.

Holland, T. J. B., Powell, R., 1998. An internally consistent thermodynamic data set for phases of petrological interest. *Journal of Metamorphic Geology*, **16(3)**, 309-343.

Holtzman, B. K., Kohlstedt, D. L., 2007. Stress-driven melt segregation and strain partitioning in partially molten rocks: Effects of stress and strain. *Journal of Petrology*, **48(12)**, 2379-2406.

Irving, A. J., 1980. Petrology and geochemistry of composite ultramafic xenoliths in alkali basalts and implications for magmatic processes within the mantle.

American Journal of Science, **280(2)**, 389-426.

Jackson, M. D., Blundy, J., Sparks, R. S. J., 2018. Chemical differentiation, cold storage and remobilization of magma in the Earth's crust. *Nature*, **564(7736)**, 405-409.

Jones, R. D. W., Katz, R. F., 2018. Reaction-infiltration instability in a compacting porous medium. *Journal of Fluid Mechanics*, **852**, 5-36.

Jordan, J. S., Hesse, M. A., Rudge, J. F., 2018. On mass transport in porosity waves. *Earth and Planetary Science Letters*, **485**, 65-78.

Katz, R. F., Spiegelman, M., Holtzman, B., 2006. The dynamics of melt and shear localization in partially molten aggregates. *Nature*, **442(7103)**, 676-679.

Kelemen, P. B., Hirth, G., Shimizu, N., Spiegelman, M., Dick, H. J. B., 1997. A review of melt migration processes in the adiabatically upwelling mantle beneath oceanic spreading ridges. *Philosophical Transactions of the Royal Society A: Mathematical, Physical and Engineering Sciences*, **355**, 283-318.

Keller, T., May, D. A., Kaus, B. J. P., 2013. Numerical modelling of magma dynamics coupled to tectonic deformation of lithosphere and crust. *Geophysical Journal International*, **195(3)**, 1406-1442.

Keller, T., Suckale, J., 2019. A continuum model of multi-phase reactive transport in igneous systems. *Geophysical Journal International*, **219(1)**, 185-222.

Korzhinskii, D., 1965. The theory of systems with perfectly mobile components and processes of mineral formation. *American Journal of Science*, **263(3)**, 193-205.

Kushiro, I., 1996. Partial melting of fertile mantle peridotite at high pressures: an experimental study using aggregates of diamond. *Geophysical Monograph-American Geophysical Union*, **95**, 109-122.

Langmuir, C. H., Klein, E. M., Plank, T., 1992. Petrological systematics of mid-ocean ridge basalts: Constraints on melt generation beneath ocean ridges. *Mantle flow and melt generation at mid-ocean ridges*, **71**, 183-280.

Lloyd, F. E., Bailey, D. K., 1975. Light element metasomatism of the continental mantle: The evidence and the consequences. *Physics and Chemistry of the Earth*, **9**, 389-416.

Malvoisin, B., Podladchikov, Y. Y., Vrijmoed, J. C., 2015. Coupling changes in densities and porosity to fluid pressure variations in reactive porous fluid flow: Local thermodynamic equilibrium. *Geochemistry, Geophysics, Geosystems*, **16(12)**, 4362-4387.

McKenzie, D., 1984. The Generation and Compaction of Partially Molten Rock. *Journal of Petrology*, **25(3)**, 713-765.

McKenzie, D., 1985. The extraction of magma from the crust and mantle. *Earth and Planetary Science Letters*, **74(1)**, 81-91.

McKenzie, D., 1989. Some remarks on the movement of small melt fractions in the mantle. *Earth and Planetary Science Letters*, **95(1-2)**, 53-72.

Miller, R. B., Paterson, S. R., 1999. In defense of magmatic diapirs. *Journal of Structural Geology*, **21(8-9)**, 1161-1173.

Müller, I., 2007. A history of thermodynamics: the doctrine of energy and entropy. *Springer Science & Business Media*.

Nauman, E. B., He, D. Q., 2001. Nonlinear diffusion and phase separation. *Chemical Engineering Science*, **20**, 1999-2018.

Nielson, J. E., Noller, J. S., 1987. Processes of mantle metasomatism; Constraints from observations of composite peridotite xenoliths. *Geological Society of America*, **215**, 61-76.

Nielson, J. E., Wilshire, H., 1993. Magma transport and metasomatism in the mantle: A critical review of current geochemical models. *American Mineralogist*, **78**, 1117-1134.

Omlin, S., Malvoisin, B., Podladchikov, Y. Y., 2017. Pore fluid extraction by reactive solitary waves in 3-d. *Geophysical Research Letters*, **44(18)**, 9267-9275.

Pilet, S., Baker, M. B., Stolper, E. M., 2008. Metasomatized lithosphere and the origin of alkaline lavas. *Science*, **320(5878)**, 916-919.

Plümper, O., John, T., Podladchikov, Y. Y., Vrijmoed, J. C., Scambelluri, M., 2016. Fluid escape from subduction zones controlled by channel-forming reactive porosity. *Nature Geoscience*, **10(2)**, 150-156.

Räss, L., Duretz, T., Podladchikov, Y. Y., 2019. Resolving hydromechanical coupling in two and three dimensions: spontaneous channelling of porous fluids owing to decompaction weakening. *Geophysical Journal International*, **218(3)**, 1591-1616.

Schmalholz, S. M., Moulas, E., Plümper, O., Myasnikov, A. V., Podladchikov, Y. Y., 2020. 2D Hydro-Mechanical-Chemical Modeling of (De)hydration Reactions in Deforming Heterogeneous Rock: The Periclase-Brucite Model Reaction. *Geochemistry, Geophysics, Geosystems*, **21(11)**.

Scott, D. R., Stevenson, D. J., 1984. Magma solitons. *Geophysical Research Letters*. **11(11)**, 1161-1164.

Shaw, H. R. 1980. The fracture mechanisms of magma transport from the mantle to the surface. *Physics of magmatic processes*, pp.201-264. Princeton Univ. Press.

Spiegelman, M., 1993. Physics of melt extraction: Theory, implications and applications. *Philosophical Transactions of the Royal Society of London. Series A: Physical and Engineering Sciences*, **342(1663)**, 23-41.

Spiegelman, M., Kelemen, P. B., Aharonov, E., 2001. Causes and consequences of flow organization during melt transport: The reaction infiltration instability

in compactible media. *Journal of Geophysical Research: Solid Earth*, **106(B2)**, 2061-2077.

Stevenson, D. J., 1989. Spontaneous small-scale melt segregation in partial melts undergoing deformation. *Geophysical Research Letters*, **16(9)**, 1067-1070.

Tomlinson, E. L., Kamber, B. S., 2021. Depth-dependent peridotite-melt interaction and the origin of variable silica in the cratonic mantle. *Nature Communications*, **12(1)**, 1082.

Walker, D., Stolper, E. M., Hays, J. F., 1978. A numerical treatment of melt/solid segregation: Size of the eucrite parent body and stability of the terrestrial low-velocity zone. *Journal of Geophysical Research: Solid Earth*, **83(B12)**, 6005-6013.

Walter, M. J., 1998. Melting of garnet peridotite and the origin of komatiite and depleted lithosphere. *Journal of Petrology*, **39(1)**, 29-60.

Wass, S. Y., Roge, N. W., 1980. Mantle metasomatism-precursor to continental alkaline volcanism. *Geochimica et Cosmochimica Acta*, **44(11)**, 1811-1823.

Wasylenki, L. E., Baker, M. B., Kent, A. J. R., Stolper, E. M., 2003. Near-solidus Melting of the Shallow Upper Mantle: Partial Melting Experiments on Depleted Peridotite. *Journal of Petrology*, **44(7)**, 1163-1191.

Weatherley, S. M., Katz, R. F., 2012. Melting and channelized magmatic flow in chemically heterogeneous, upwelling mantle. *Geochemistry, Geophysics, Geosystems*, **13(5)**.

Weinberg, R. F., Podladchikov, Y., 1994. Diapiric ascent of magmas through power law crust and mantle. *Journal of Geophysical Research: Solid Earth*, **99(B5)**, 9543-9559.

Wilshire, H., 1987. A model of mantle metasomatism. *Mantle Metasomatism and Alkaline Magmatism. Geological Society of America, Special Papers*, **215**, 47-60.

Yarushina, V. M., Podladchikov, Y. Y., 2015. (De)compaction of porous viscoelastoplastic media: Model formulation. *Journal of Geophysical Research: Solid Earth*, **120 (6)**, 4146-4170.

Appendix A. THMC model equations

A general conservation equation without a source term in 1D for any variable, here named B (per unit volume), has the form:

$$\frac{\partial B}{\partial t} = -\frac{\partial}{\partial x} q_A - \frac{\partial}{\partial x} q_D \quad \text{(A1)}$$

where t is the time, q_A is the advective flux and q_D is the diffusive flux. The

advective flux corresponds to the transport of B with its velocity v_b:

$$q_A = Bv_b \quad \text{(A2)}$$

A porous medium, with porosity φ, is composed of a solid skeleton (solid phase) with density ρ_s and a melt phase in the pores with density ρ_m. The total mass of the medium, having total density ρ_T, is the sum of the mass of melt in pores and the mass of the solid:

$$B = \rho_m\varphi + \rho_s(1-\varphi) = \rho_T \quad \text{(A3)}$$

The advective flux for the total mass is:

$$q_A = \rho_m\varphi v_m + \rho_s(1-\varphi)v_s \quad \text{(A4)}$$

where v_m and v_s are the melt and solid velocities, respectively. There is no diffusive flux in the conservation of the total mass, hence:

$$q_D = 0 \quad \text{(A5)}$$

Therefore, the conservation equation for total mass is:

$$\frac{\partial}{\partial t}\left(\rho_m\varphi + \rho_s(1-\varphi)\right) = -\frac{\partial}{\partial x}\left(\rho_m\varphi v_m + \rho_s(1-\varphi)v_s\right) \quad \text{(A6)}$$

The force balance for the melt follows Darcy's law:

$$\varphi\left(v_m - v_s\right) = -\frac{k\varphi^3}{\eta_m}\left(\frac{\partial P_m}{\partial x} + \rho_m g\right) \quad \text{(A7)}$$

where k is the permeability, η_m is the melt viscosity, P_m is the melt pressure and g is the gravitational acceleration. To introduce the Darcy's force balance in the total mass conservation equation, it is useful to modify equation (A6) by subtracting and adding v_s to v_m:

$$\frac{\partial}{\partial t}\left(\rho_m\varphi + \rho_s(1-\varphi)\right) = -\frac{\partial}{\partial x}\left(\rho_m\varphi(v_m - v_s + v_s) + \rho_s(1-\varphi)v_s\right) \quad \text{(A8)}$$

Equation (A8) can be rewritten as:

$$\frac{\partial}{\partial t}\left(\rho_m\varphi+\rho_s(1-\varphi)\right)=-\frac{\partial}{\partial x}\left(-\rho_m\frac{k\varphi^3}{\eta_m}\left(\frac{\partial P_m}{\partial x}+\rho_m g\right)+\rho_m\varphi v_s+\rho_s(1-\varphi)v_s\right) \quad \text{(A9)}$$

Equation (A9) can be simplified by collecting terms in front of v_s:

$$\frac{\partial}{\partial t}\left(\rho_m\varphi+\rho_s(1-\varphi)\right)=-\frac{\partial}{\partial x}\left(-\rho_m\frac{k\varphi^3}{\eta_m}\left(\frac{\partial P_m}{\partial x}+\rho_m g\right)+\rho_T v_s\right) \quad \text{(A10)}$$

The total mass of magnesium (MgO) considers the concentration of MgO in the melt and in the solid:

$$B=C_m^{\mathrm{MgO}}\rho_m\varphi+C_s^{\mathrm{MgO}}\rho_s(1-\varphi)=M_T^{\mathrm{MgO}} \quad \text{(A11)}$$

where C_m^{MgO} and C_s^{MgO} are, respectively, the mass fractions (C_m^{MgO} = mass of MgO in the melt / total mass of melt; C_s^{MgO} = mass of MgO in the solid / total mass of solid) of MgO in the melt and in the solid. The advective flux for the total mass of MgO is:

$$q_A=C_m^{\mathrm{MgO}}\rho_m\varphi v_m+C_s^{\mathrm{MgO}}\rho_s(1-\varphi)v_s \quad \text{(A12)}$$

Assuming an ideal solution, the diffusive flux is described by Fick's law that describes the molecular diffusion of MgO in the melt and in the solid:

$$q_D=-D_m^{\mathrm{MgO}}\rho_m\varphi\frac{\partial C_m^{\mathrm{MgO}}}{\partial x}-D_s^{\mathrm{MgO}}\rho_s(1-\varphi)\frac{\partial C_s^{\mathrm{MgO}}}{\partial x} \quad \text{(A13)}$$

where D_m^{MgO} and D_s^{MgO} are the effective diffusivities of MgO in the melt and in the solid (e.g. Naumann and He, 2001). Therefore, the conservation equation for total mass of MgO is:

$$\frac{\partial}{\partial t}\left(C_m^{\mathrm{MgO}}\rho_m\varphi+C_s^{\mathrm{MgO}}\rho_s(1-\varphi)\right)=-\frac{\partial}{\partial x}\left(C_m^{MgO}\rho_m\varphi v_m+C_s^{\mathrm{MgO}}\rho_s(1-\varphi)v_s-D_m^{\mathrm{MgO}}\rho_m\varphi\frac{\partial C_m^{\mathrm{MgO}}}{\partial x}-D_s^{\mathrm{MgO}}\rho_s(1-\right.$$

The total mass per unit of volume SiO_2 considers the concentration of SiO_2 in the melt and in the solid:

$$B = C_m^{SiO_2}\rho_m\varphi + C_s^{SiO_2}\rho_s(1-\varphi) = M_T^{SiO_2} \quad \text{(A15)}$$

where $C_m^{SiO_2}$ and $C_s^{SiO_2}$ are respectively the mass fractions ($C_m^{SiO_2}$ = mass of SiO_2 in the melt / total mass of melt; $C_s^{SiO_2}$ = mass of SiO_2 in the solid / total mass of solid) of SiO_2 in the melt and in the solid. The advective flux for the total mass of SiO_2 is:

$$q_A = C_m^{SiO_2}\rho_m\varphi v_m + C_s^{SiO_2}\rho_s(1-\varphi)v_s \quad \text{(A16)}$$

For an ideal solution, the diffusive flux is described by Fick's law that describes the molecular diffusion of SiO_2 in the melt and in the solid:

$$q_D = -D_m^{SiO_2}\rho_m\varphi\frac{\partial C_m^{SiO_2}}{\partial x} - D_s^{SiO_2}\rho_s(1-\varphi)\frac{\partial C_s^{SiO_2}}{\partial x} \quad \text{(A17)}$$

where $D_m^{SiO_2}$ and $D_s^{SiO_2}$ are the effective diffusivities of SiO_2 in the melt and in the solid (e.g. Naumann and He, 2001). Therefore, conservation equation for total mass of SiO_2 is:

$$\frac{\partial}{\partial t}\left(C_m^{SiO_2}\rho_m\varphi + C_s^{SiO_2}\rho_s(1-\varphi)\right) = -\frac{\partial}{\partial x}\left(C_m^{SiO_2}\rho_m\varphi v_m + C_s^{SiO_2}\rho_s(1-\varphi)v_s - D_m^{SiO_2}\rho_m\varphi\frac{\partial C_m^{SiO_2}}{\partial x} - D_s^{SiO_2}\rho_s(1-\right.$$

The total thermal energy of the medium is:

$$U_m(P,T) = \int_{T_{\text{ref}}}^{T}\left(c_{p_m}\left(P,T'\right)\rho_m\left(P,T'\right)\right)dT' \quad \text{(A19)}$$

$$U_s(P,T) = \int_{T_{\text{ref}}}^{T}\left(c_{p_s}\left(P,T'\right)\rho_s\left(P,T'\right)\right)dT'$$

$$B = U_m\varphi + U_s(1-\varphi) = U_T$$

where c_{p_m} and c_{p_s} are specific heat capacity of the melt and the solid and T is the temperature. The advective flux for thermal energy is:

$$q_A = U_m\varphi v_m + U_s(1-\varphi)v_s \quad \text{(A20)}$$

Assuming that the temperature in the solid and fluid is identical, the diffusive

flux is described by Fourier'law:

$$q_D = -\lambda_T \frac{\partial T}{\partial x} \quad \text{(A21)}$$

where $\lambda_T = (\lambda_m \varphi + \lambda_s (1 - \varphi))$ and λ_m and λ_s are the thermal conductivity of melt and solid, respectively. The conservation equation for the energy takes the form of:

$$\frac{\partial}{\partial t} \left(U_m \varphi + U_s (1 - \varphi) \right) = -\frac{\partial}{\partial x} \left(U_m \varphi v_m + U_s (1 - \varphi) v_s - \lambda_T \frac{\partial T}{\partial x} \right) \quad \text{(A22)}$$

The other mechanical equations that close the system of equations are presented in section 2.2, equations 12, 13, 15 and 16.

Appendix B. Additional figures and tables

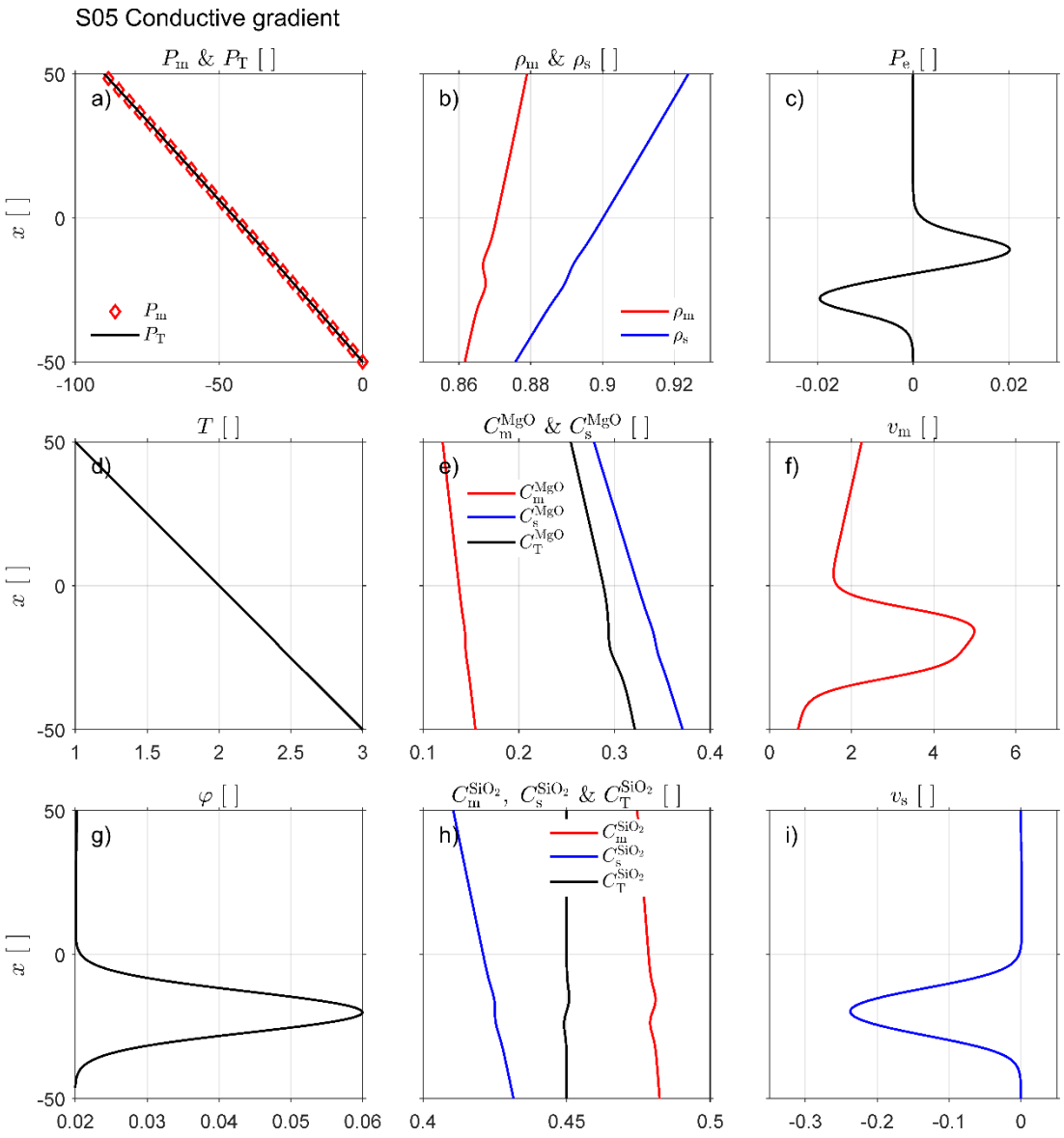

Figure B12. Initial profiles of simulation S05 Conductive gradient, all variables are dimensionless. Panel (a) shows melt pressure (red diamond) and total pressure (black line). Panel (b) shows melt density (red line) and solid density (blue line). Panel (c) shows effective pressure, positive values indicate decompaction while negative values indicate compaction. Panel (d) shows temperature. Panel

(e) shows magnesium mass fraction in melt (red line) and in solid (blue line) and total magnesium mass fraction (black line). Panel (f) shows melt velocity. Panel (g) shows porosity. Panel (h) shows silica mass fraction in melt (red line) and in the solid (blue line) and total silica mass fraction (black line). Panel (i) shows solid velocity.

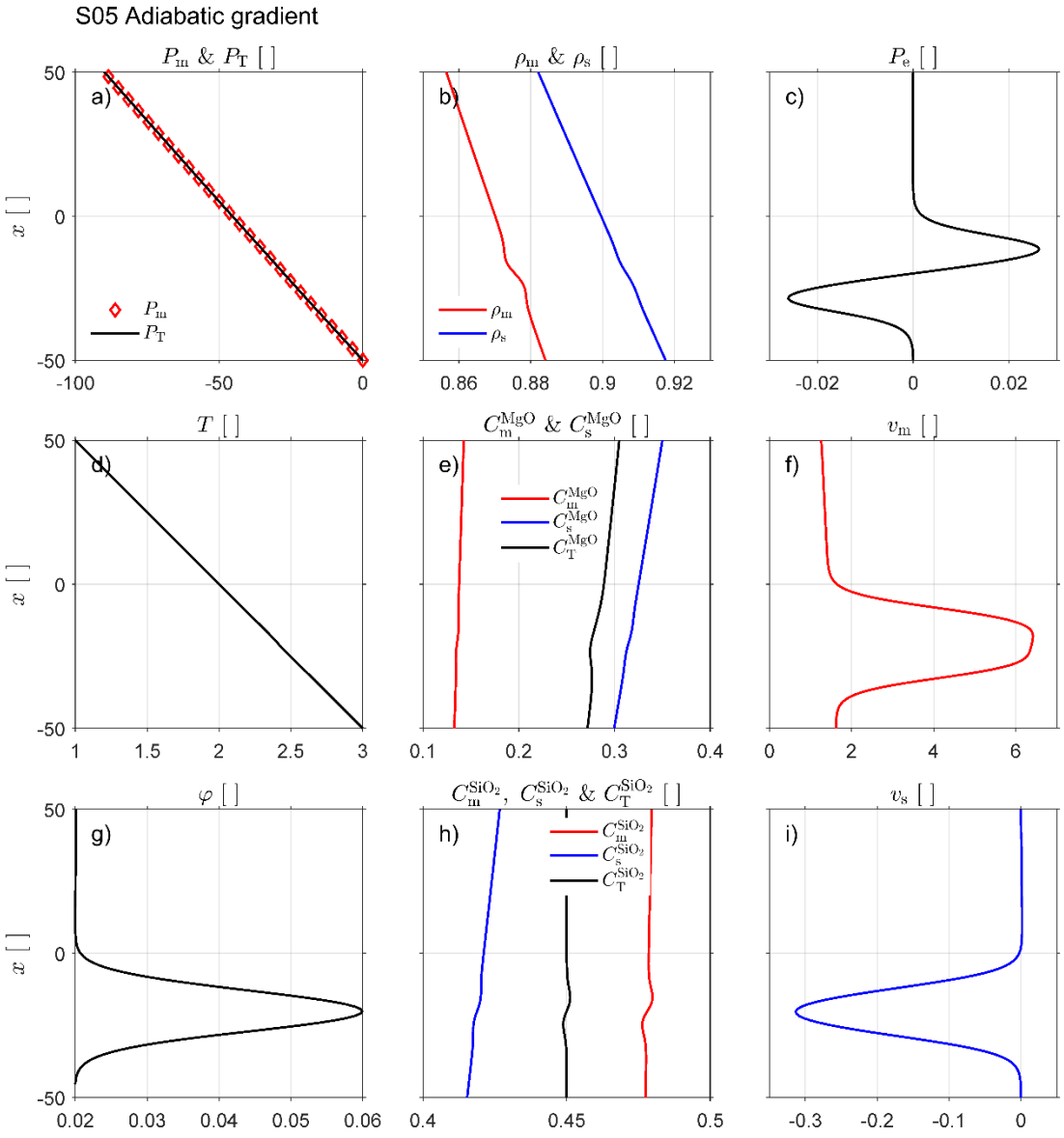

Figure B13. Initial profiles of simulation S05 Adiabatic gradient, all variables are

dimensionless. Panel (a) shows melt pressure (red diamond) and total pressure (black line). Panel (b) shows melt density (red line) and solid density (blue line). Panel (c) shows effective pressure, positive values indicate decompaction while negative values indicate compaction. Panel (d) shows temperature. Panel (e) shows magnesium mass fraction in melt (red line) and in solid (blue line) and total magnesium mass fraction (black line). Panel (f) shows melt velocity. Panel (g) shows porosity. Panel (h) shows silica mass fraction in melt (red line) and in the solid (blue line) and total silica mass fraction (black line). Panel (i) shows solid velocity.

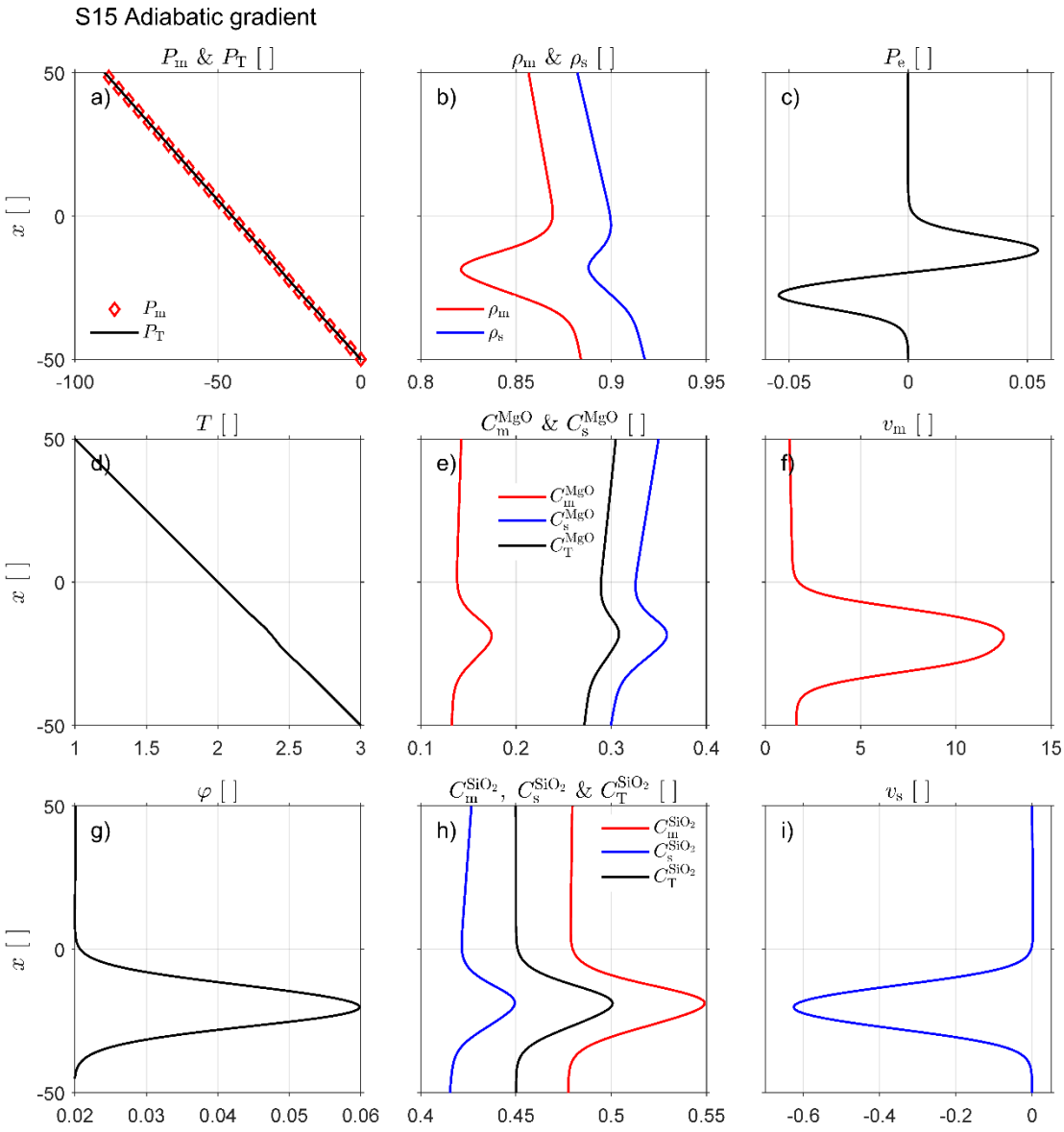

Figure B14. Initial profiles of simulation S15 Adiabatic gradient, all variables are dimensionless. Panel (a) shows melt pressure (red diamond) and total pressure (black line). Panel (b) shows melt density (red line) and solid density (blue line). Panel (c) shows effective pressure, positive values indicate decompaction while negative values indicate compaction. Panel (d) shows temperature. Panel (e) shows magnesium mass fraction in melt (red line) and in solid (blue line)

and total magnesium mass fraction (black line). Panel (f) shows melt velocity. Panel (g) shows porosity. Panel (h) shows silica mass fraction in melt (red line) and in the solid (blue line) and total silica mass fraction (black line). Panel (i) shows solid velocity.

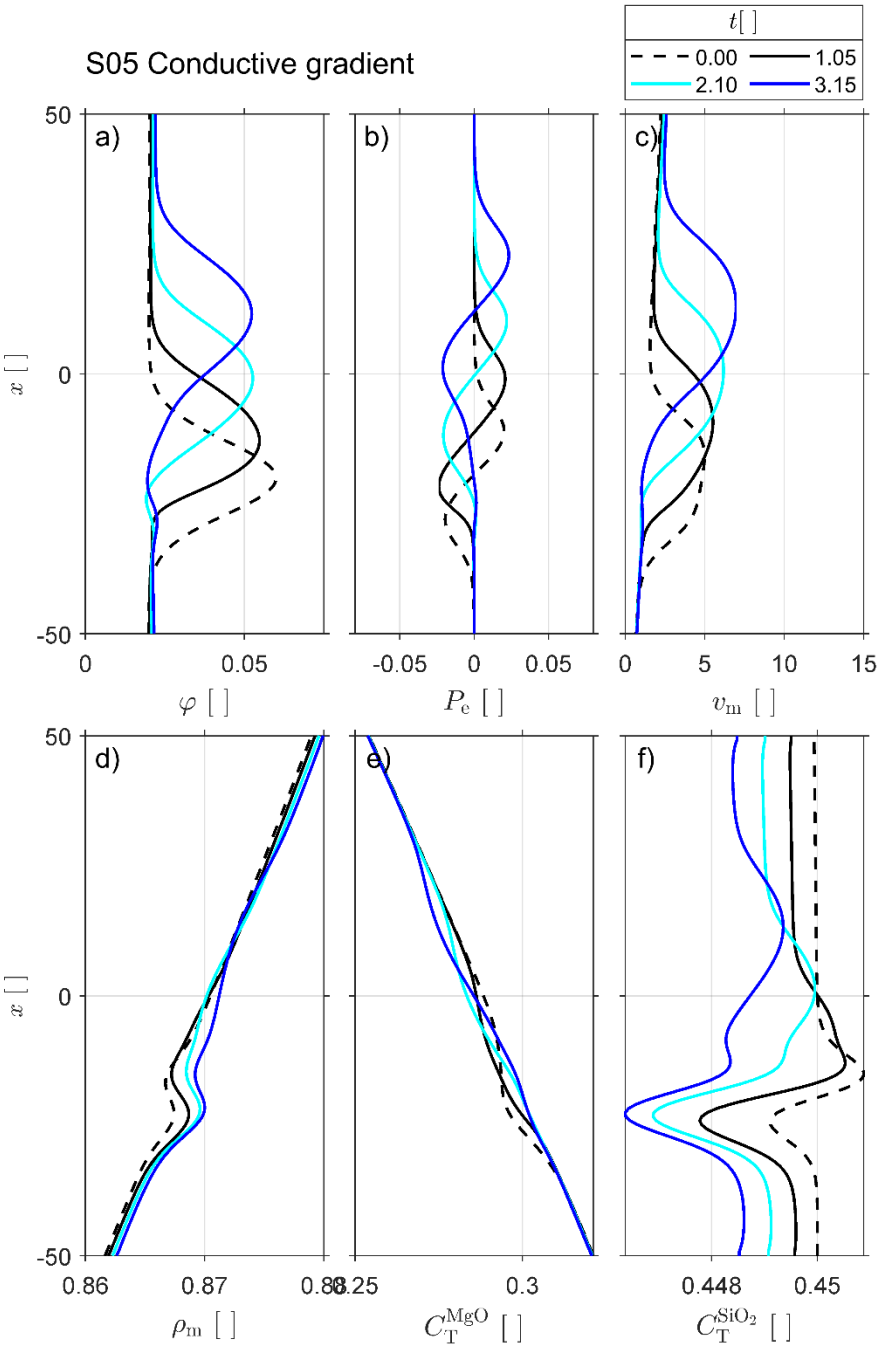

Figure B15. Evolution in time of six variables in simulation S05 Conductive gradient, all variables are dimensionless. Panel (a) shows porosity, panel (b)

shows effective pressure, panel (c) shows melt velocity, panel (d) shows melt density, panel (e) shows total magnesium mass fraction and panel (f) shows total silica mass fraction. Four time steps are chosen at different dimensional times: t = 0 with dashed line (corresponding to the initial profiles in figure B12 for each variables), t = 1.05 with black line, t = 2.10 with light blue and t = 3.15 with dark blue (see legend).

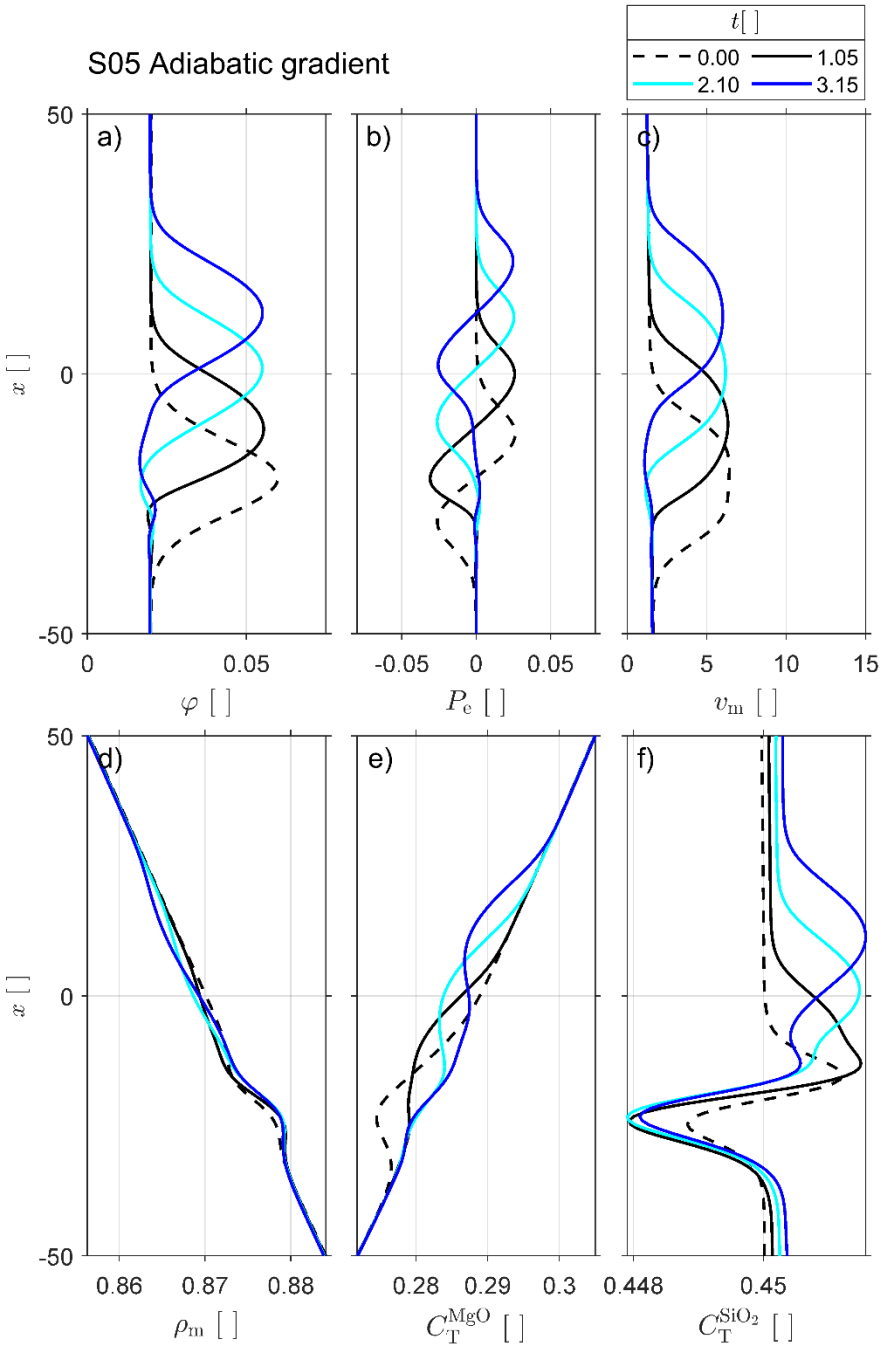

Figure B16. Evolution in time of six variables in simulation S05 Adiabatic gradient, all variables are dimensionless Panel (a) shows porosity, panel (b)

shows effective pressure, panel (c) shows melt velocity, panel (d) shows melt density, panel (e) shows total magnesium mass fraction and panel (f) shows total silica mass fraction. Four time steps are chosen at different dimensional times: t = 0 with dashed line (corresponding to the initial profiles in figure B13 for each variables), t = 1.05 with black line, t = 2.10 with light blue and t = 3.15 with dark blue (see legend).

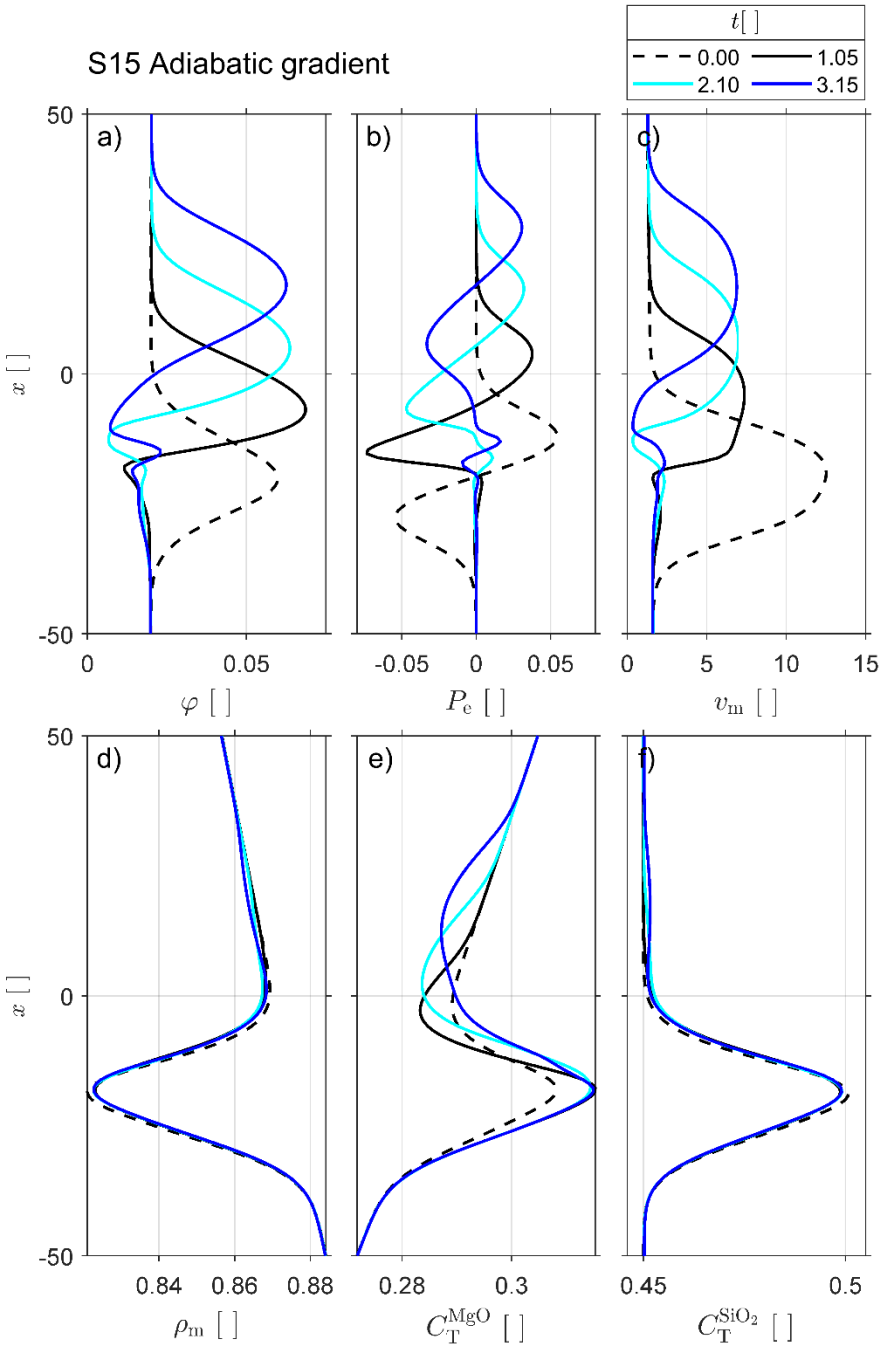

Figure B17. Evolution in time of six variables in simulation S15 Adiabatic gradient, all variables are dimensionless. Panel (a) shows porosity, panel (b)

shows effective pressure, panel (c) shows melt velocity, panel (d) shows melt density, panel (e) shows total magnesium mass fraction and panel (f) shows total silica mass fraction. Four time steps are chosen at different dimensional times: t = 0 with dashed line (corresponding to the initial profiles in figure B14 for each variables), t = 1.05 with black line, t = 2.10 with light blue and t = 3.15 with dark blue (see legend).

Table B3. Numerical pseudo-transient time step used in the THMC simulations

Pseudo-transient time step	
for the melt pressure	${t_P}^{\mathrm{TP}} = \frac{1}{2}\frac{\mathrm{dx}^2}{\max\left(\frac{k}{\eta_m}\cdot\left(\frac{\varphi}{\varphi_0}\right)^3\right)}$
for the porosity	${t_\varphi}^{\mathrm{TP}} = \mathrm{dt}$
for the total silica content	${t_{C_T^{\mathrm{Si}O_2}}}^{\mathrm{TP}} = \mathrm{dt}$
for the temperature	${t_T}^{\mathrm{TP}} = \frac{1}{4.1}\frac{\mathrm{dx}^2}{\max\left(\frac{\lambda_m}{\rho_T {c_p}_T}\right)}$
for the solid velocity	${t_{v_s}}^{\mathrm{TP}} = \frac{1}{6}\frac{\mathrm{dx}^2}{\eta_s}$

Appendix C. Thermodynamic calculations

Transformation from molar fractions into mass fractions

To use molar concentrations in the mass conservation equations of the THMC transport model, we first transform these concentrations into olivine phase mass fractions:

$$C_m^{\mathrm{foL}} = \frac{C_{m,[\mathrm{mol}]}^{\mathrm{foL}}\cdot m_m^{\mathrm{foL}}}{\left(C_{m,\ [\mathrm{mol}]}^{\mathrm{foL}}\cdot m_m^{\mathrm{foL}}\right)+\left(C_{m,[\mathrm{mol}]}^{\mathrm{faL}}\cdot m_m^{\mathrm{faL}}\right)} \quad \text{(C1a)}$$

$$C_m^{\mathrm{faL}} = \frac{C_{m,[mol]}^{\mathrm{faL}}\cdot m_m^{\mathrm{faL}}}{\left(C_{m,[\mathrm{mol}]}^{\mathrm{foL}}\cdot m_m^{\mathrm{foL}}\right)+\left(C_{m,[\mathrm{mol}]}^{\mathrm{faL}}\cdot m_m^{\mathrm{faL}}\right)} \quad \text{(C1b)}$$

$$C_s^{\mathrm{fo}} = \frac{C_{s,[mol]}^{\mathrm{fo}}\cdot m_s^{\mathrm{fo}}}{\left(C_{s,[\mathrm{mol}]}^{\mathrm{fo}}\cdot m_s^{\mathrm{fo}}\right)+\left(C_{s,[\mathrm{mol}]}^{\mathrm{fa}}\cdot m_s^{\mathrm{fa}}\right)} \quad \text{(C1c)}$$

$$C_s^{\mathrm{fa}} = \frac{C_{s,[mol]}^{\mathrm{fa}}\cdot m_s^{\mathrm{fa}}}{\left(C_{s,[\mathrm{mol}]}^{\mathrm{fo}}\cdot m_s^{\mathrm{fo}}\right)+\left(C_{s,[\mathrm{mol}]}^{\mathrm{fa}}\cdot m_s^{\mathrm{fa}}\right)} \quad \text{(C1d)}$$

where m_m^{foL}, m_m^{faL}, m_s^{fo} and m_s^{fa} are, respectively, the molar mass of forsterite and fayalite liquid for the melt part and forsterite and fayalite for the solid part. We transform these olivine phase mass fractions into oxide mass fractions of MgO, FeO and SiO_2:

$$C_{m,i}^{\mathrm{MgO}} = C_m^{\mathrm{foL}}\cdot M_r^{\mathrm{MgO}}\cdot \mathrm{nb}^{\mathrm{MgO}} \quad \text{(C2a)}$$

$$C_{m,i}^{\mathrm{FeO}} = (1-C_m^{\mathrm{foL}})\cdot M_r^{\mathrm{FeO}}\cdot \mathrm{nb}^{\mathrm{FeO}} \quad \text{(C2b)}$$

$$C_{m,i}^{\mathrm{Si}O_2} = (C_m^{\mathrm{foL}}+1-C_m^{\mathrm{foL}})\cdot M_r^{\mathrm{Si}O_2}\cdot \mathrm{nb}^{\mathrm{Si}O_2} \quad \text{(C2c)}$$

where M_r^{MgO}, M_r^{FeO} and $M_r^{\mathrm{SiO_2}}$ are molecular weight (i.e. relative molecular mass) of oxides ($M_r^{\mathrm{MgO}} = 0.0403$ [kg $\cdot$ mol^{-1}], $M_r^{\mathrm{FeO}} = 0.0708$ [kg $\cdot$ mol^{-1}] and $M_r^{\mathrm{SiO_2}} = 0.0601$ [kg $\cdot$ mol^{-1}]), $\mathrm{nb}^{\mathrm{MgO}}$, $\mathrm{nb}^{\mathrm{FeO}}$ and $\mathrm{nb}^{\mathrm{SiO_2}}$ correspond to the number of times each oxide is in the olivine formula ($\mathrm{nb}^{\mathrm{MgO}} = \mathrm{nb}^{\mathrm{FeO}} = 2$ and $\mathrm{nb}^{\mathrm{SiO_2}} = 1$), subscript i indicates that the oxide mass fractions $C_{m,i}^{\mathrm{MgO}}$, $C_{m,i}^{\mathrm{FeO}}$ and $C_{m,i}^{\mathrm{SiO_2}}$ are not normalised. For the normalization, each oxide mass fraction is divided by the sum of these three oxide mass fractions:

$$C_m^{\mathrm{MgO}} = \frac{C_{m,i}^{\mathrm{MgO}}}{C_{m,i}^{\mathrm{MgO}} + C_{m,i}^{\mathrm{FeO}} + C_{m,i}^{\mathrm{SiO_2}}} \quad \text{(C3a)}$$

$$C_m^{\mathrm{FeO}} = \frac{C_{m,i}^{\mathrm{FeO}}}{C_{m,i}^{\mathrm{MgO}} + C_{m,i}^{\mathrm{FeO}} + C_{m,i}^{\mathrm{SiO_2}}} \quad \text{(C3b)}$$

$$C_m^{\mathrm{SiO_2}} = \frac{C_{m,i}^{\mathrm{SiO_2}}}{C_{m,i}^{\mathrm{MgO}} + C_{m,i}^{\mathrm{FeO}} + C_{m,i}^{\mathrm{SiO_2}}} \quad \text{(C3c)}$$

C_m^{MgO}, C_m^{FeO} and $C_m^{\mathrm{SiO_2}}$ are the oxide mass fractions that we use in the THMC model. We proceed with the same approach to calculate the values for the solid part, C_s^{MgO}, C_s^{FeO} and $C_s^{\mathrm{SiO_2}}$.

Calculation of γ

We calculate the γ for $C_m^{\mathrm{SiO_2}}$ and $C_s^{\mathrm{SiO_2}}$ as follow :

$$\gamma_{C_m^{\mathrm{SiO_2}}} = \frac{\left(\frac{C_{m,exp}^{\mathrm{SiO_2}} - C_{m,0}^{\mathrm{SiO_2}}}{C_{T,exp}^{\mathrm{SiO_2}} - C_{T,0}^{\mathrm{SiO_2}}} \right)}{C_{m,0}^{\mathrm{SiO_2}}} \quad \text{(C4a)}$$

$$\gamma_{C_s^{\mathrm{SiO_2}}} = \frac{\left(\frac{C_{s,exp}^{\mathrm{SiO_2}} - C_{s,0}^{\mathrm{SiO_2}}}{C_{T,exp}^{\mathrm{SiO_2}} - C_{T,0}^{\mathrm{SiO_2}}} \right)}{C_{s,0}^{\mathrm{SiO_2}}} \quad \text{(C4b)}$$

For the density calculation, we use the thermodynamic data of Holland & Powell (1998) and the different minerals and liquids Mg-Fe end-members are recalculated from experimental data of Davis et al. (2011). In these calculations, we use the following end-members: for the solid part, forsterite (fo) ($\mathrm{Mg_2SiO_4}$) and fayalite (fa) ($\mathrm{Fe_2SiO_4}$) for olivine; enstatite (en) ($\mathrm{Mg_2Si_2O_6}$) and ferrosilite (fs) ($\mathrm{Fe_2Si_2O_6}$) for orthopyroxene; diopside (di) ($\mathrm{CaMgSi_2O_6}$) and hedenbergite (hed) ($\mathrm{CaFeSi_2O_6}$) for clinopyroxene; pyrope (py) ($\mathrm{Mg_3Al_2Si_3O_{12}}$) and almandine (alm) ($\mathrm{Fe_3Al_2Si_3O_{12}}$) for garnet. We consider also quartz (q) ($\mathrm{SiO_2}$). For the melt part, we consider forsterite liquid (foL), fayalite liquid (faL) and quartz liquid (qL). The abbreviations in brackets correspond to the nomenclature of Holland & Powell (1998).